



Molecular-scale description of interfacial mass transfer in phase-separated aqueous secondary organic aerosol

Mária Lbadaoui-Darvas¹, Satoshi Takahama¹, and Athanasios Nenes^{1,2}

¹Laboratory of Atmospheric Processes and their Impacts, School of Architecture, Civil and Environmental Engineering, Swiss Federal Institute of Technology, 1015 Lausanne, Switzerland

²Center of Studies on Air quality and Climate Change, Institute of Chemical Engineering Sciences, Foundation for Research and Technology Hellas, Patras, 26504, Greece

Correspondence: Athanasios Nenes (athanasios.nenes@epfl.ch) and Satoshi Takahama (satoshi.takahama@epfl.ch)

Received: 10 June 2021 – Discussion started: 17 June 2021

Revised: 20 September 2021 – Accepted: 7 October 2021 – Published: 3 December 2021

Abstract. Liquid–liquid phase-separated (LLPS) aerosol particles are known to exhibit increased cloud condensation nuclei (CCN) activity compared to well-mixed ones due to a complex effect of low surface tension and non-ideal mixing. The relation between the two contributions as well as the molecular-scale mechanism of water uptake in the presence of an internal interface within the particle is to date not fully understood. Here we attempt to gain understanding in these aspects through steered molecular dynamics simulation studies of water uptake by a vapor–hydroxy-*cis*-pinonic acid–water double interfacial system at 200 and 300 K. Simulated free-energy profiles are used to map the water uptake mechanism and are separated into energetic and entropic contributions to highlight its main thermodynamic driving forces. Atmospheric implications are discussed in terms of gas–particle partitioning, intraparticle water redistribution timescales and water vapor equilibrium saturation ratios. Our simulations reveal a strongly temperature-dependent water uptake mechanism, whose most prominent features are determined by local extrema in conformational and orientational entropies near the organic–water interface. This results in a low core uptake coefficient ($k_{o/w} = 0.03$) and a concentration gradient of water in the organic shell at the higher temperature, while entropic effects are negligible at 200 K due to the association-entropic-term reduction in the free-energy profiles. The concentration gradient, which results from non-ideal mixing – and is a major factor in increasing LLPS CCN activity – is responsible for maintaining liquid–liquid phase separation and low surface tension even at very high relative humidities, thus reducing critical supersaturations. Thermodynamic

driving forces are rationalized to be generalizable across different compositions. The conditions under which single uptake coefficients can be used to describe growth kinetics as a function of temperature in LLPS particles are described.

1 Introduction

Aerosol–cloud interactions constitute one of the most important sources of uncertainty in assessments of anthropogenic climate change (IPCC, 2021). The number, size and composition characteristics of aerosol influence the number of droplets that can form in cloudy updrafts, which in turn affect the microphysical evolution and radiative properties of clouds and affect climate. Cloud droplets form upon a subset of aerosol, called cloud condensation nuclei (CCN), that becomes unstable and experiences unconstrained growth in the supersaturated water vapor that develops in a cloudy updraft. The dynamics of water uptake on CCN is a critical process that influences the level of supersaturation that can develop in clouds (Raatikainen et al., 2013) and is affected by the interplay of gas-to-particle transport, interfacial mass transfer and diffusion in the particle phase. Water uptake by particles is controlled by the gas-to-particle transport timescale when the mean free path of gas-phase molecules is smaller than the particle size. Particle-phase diffusion dominates in glassy and semisolid aerosol, while interfacial mass transfer can be important when the particle size is comparable to or smaller than the gas-phase mean free path.

Limitations on particle growth by interfacial mass transfer can be expressed in terms of the mass accommodation coefficient (α), defined as the ratio of molecules absorbed by the particle over the total number of molecules colliding with the surface: $\alpha \sim 1$ for particles whose surface is composed of dominantly water (Clement et al., 1996; Morita et al., 2004; Voigtländer et al., 2007), while α can be very reduced for hydrophobic surfaces. For hydrophobic organic films (e.g., long chained alcohol) model film α was found to be as low as 10^{-3} to 10^{-5} from molecular dynamics (Takahama and Russell, 2011; Ergin and Takahama, 2016; Johansson et al., 2020) and experimental studies (Diveky et al., 2019; Johansson et al., 2020). Gas-to-particle partitioning on secondary organic aerosol (SOA), which constitutes a significant fraction of the total particulate matter on a global scale (Fuzzi et al., 2006), is usually characterized by $\alpha > 0.1$ (Raatikainen et al., 2013; Julin et al., 2014; Krechmer et al., 2017). Modeling studies have long shown that reduced mass accommodation coefficients result in an increased droplet number concentration in clouds, owing to the slow condensation of water vapor in the initial stages of cloud formation, which in turn elevates supersaturation and allows for more CCN to activate. For these kinetic delays to be important for climate simulations, the uptake coefficient needs to be less than 0.1 (Raatikainen et al., 2013). To date, although low values of α have been reported for select systems, analysis of droplet formation upon aerosol from a broad range of environments – even aerosol with large amounts of hydrophobic material (Moore et al., 2012; Raatikainen et al., 2013) – has not indicated uptake coefficients below 0.1. α also depends on temperature in a system-specific way (Li et al., 2001; Davidovits et al., 2004; Zientara et al., 2008; Davies et al., 2013; Roy et al., 2020). This is typically not accounted for by parcel models of cloudy updrafts, which tend to use a single α value to simulate the entire range in which the temperature of a rising air parcel varies (Morales Betancourt and Nenes, 2014) and can lead to systematic errors, whose magnitude may depend on elevation (i.e., as temperature drops).

While the single parameter description, which uses only the mass accommodation coefficient to describe gas-to-particle partitioning in atmospheric systems, is established, in reality the definition of α is somewhat unambiguous. A definition of the reference state – i.e., the state beyond which a water molecule is considered to have partitioned to the particle phase – is unclear. The most commonly accepted definition of α uses adsorption at the particle surface or absorption by the first few molecular layers of the particle as a reference state, while a penetration-depth-dependent definition (Shiraiwa and Pöschl, 2020) has also been proposed. The latter accounts for particle-phase diffusion using an effective accommodation coefficient. This approach turns out to be sufficiently complex to describe water uptake by well-mixed particles.

Typical values of $\alpha > 0.1$ observed for SOA CCN suggest that they do not substantially exhibit kinetic delays in

gas-to-particle partitioning. Nevertheless, increased CCN activity compared to the one predicted by κ -Köhler theory has been reported for SOA in particular for liquid–liquid phase-separated (LLPS) particles (Prenni et al., 2007; Pajunoja et al., 2015; Liu et al., 2018). Liquid–liquid phase separation tends to occur in deliquesced SOA-rich aerosol if the O : C ratio of the organics is below 0.8 (Song et al., 2012, 2017; Renbaum-Wolff et al., 2016). Particles formed by liquid–liquid phase separation have either core–shell or partially engulfed morphologies (Song et al., 2012; You et al., 2014; Gorkowski et al., 2020). LLPS organic shells are non-ideal mixed multilayers, potentially affecting interfacial mass transfer kinetics in a complex way which may possibly not be parametrized by a single mass accommodation coefficient (Krieger et al., 2012; Davies et al., 2013). Increased CCN activity of LLPS particles may arise from (i) reduced surface tension due to the high concentrations of organic molecules at the surface of LLPS particles, (ii) surface adsorption (Pajunoja et al., 2015; Sareen et al., 2013) or (iii) non-ideal mixing. Surface tension reduction has been proven in laboratory (Song et al., 2012, 2017; Renbaum-Wolff et al., 2016) and field (Facchini et al., 1999) experiments, and its role in enhancing CCN activity has been extensively discussed (Ruehl et al., 2012, 2016; Nozière, 2016; Ovadnevaite et al., 2017). The existence of long-lived surface-adsorbed states is unlikely when the outer phase has randomly oriented hydrophobic groups, due to the rapid formation of H bonds seen in molecular dynamics (MD) simulations (Johansson et al., 2020), and was recently experimentally shown to be insignificant (Liu et al., 2018). Studies have also shown the importance of non-Raoult-type non-ideality by introducing a Flory–Huggins type of representation of the non-ideal Gibbs free energy of mixing in a κ -Köhler model (Petters et al., 2006; Liu et al., 2018). However, Flory–Huggins theory cannot explain how such non-idealities can enhance CCN activity. Molecular-scale understanding of the manifestation of non-idealities in the particle structure can help in understanding how reduced surface tension and non-ideal mixing effects are linked.

Both the ambiguities surrounding the definition of gas-to-particle partitioning in particles that are not well mixed and the lack of detailed understanding of the effect of liquid–liquid phase separation on cloud droplet growth and activation are closely tied to the limited molecular-scale knowledge about the partitioning process, which has been mapped for only a handful of systems (Sakaguchi and Morita, 2012; Ergin and Takahama, 2016). Nanosecond timescales associated with interfacial mass transfer of a single water molecule to an aerosol particle (Bzdek and Reid, 2017) are conveniently studied by MD simulations, using equilibrium (Bahadur and Russell, 2008), direct-impinging (Vieceli et al., 2005; Takahama and Russell, 2011; Johansson et al., 2020) or umbrella-sampling (Sakaguchi and Morita, 2012; Ergin and Takahama, 2016) techniques. They have estimated near-unity surface accommodation coefficients on pure water surfaces (Morita

et al., 2004; Viecei et al., 2005; Takahama and Russell, 2011) and have reproduced reduced coefficients characteristic of hydrophobic surfaces (Sakaguchi and Morita, 2012; Ergin and Takahama, 2016; Miles et al., 2016; Johansson et al., 2020) as well as the size dependence of the uptake coefficient in salt nanoparticles (Bahadur and Russell, 2008). In direct-impinging simulations, gas-phase molecules are launched with an initial velocity towards the bulk phase in several trials and the mass accommodation coefficient is simply estimated as the ratio of successful trials. This method requires additional techniques to identify the eventual fate of molecules that are adsorbed at the surface but desorbed later without entering the bulk liquid phase. Umbrella-sampling (Torrie and Valleau, 1977) simulations are used to reconstruct the free-energy profile of water uptake from a series of equilibrium simulations with the position of the gas-phase molecule at different distances from the bulk, which is then converted to the mass accommodation coefficient using transition state theory (Sakaguchi and Morita, 2012). In its traditional formulation, umbrella sampling used to study transfer through liquid surfaces artificially smoothes the effect of thermal surface fluctuations due to the way in which averaging is performed (Darvas et al., 2013). A very recent study used well-tempered metadynamics to estimate equilibrium partitioning coefficients of volatile organics (von Domaros et al., 2020). In this work, an alternative approach based on steered molecular dynamics (Park and Schulten, 2004) is proposed. It has been successful at exploring free-energy profiles using out-of-equilibrium simulations along distance-related reaction coordinates in biophysical contexts (e.g., Allen et al., 2014).

This paper presents a molecular simulation study aimed at revealing the mechanism of water uptake in a vapor-hydroxy-*cis*-pinonic acid–water double interfacial system at two temperatures, characteristic of the planetary boundary layer and the upper troposphere. Free-energy profiles of water uptake are generated using steered MD simulations and are used to describe the temperature dependence of the water uptake mechanism. Thermodynamic driving forces are identified by decomposing the free-energy profiles into entropic and energetic contributions, and the causality between the exact molecular-scale representation of non-ideal mixing thermodynamics and observed increased CCN activities is inferred from the thermodynamic description. Knowing the molecular-scale mechanism of water uptake, the usability of a single mass accommodation coefficient to describe gas-to-particle partitioning is assessed by modeling characteristic timescales and concentration distributions in the organic shell. Finally, different scenarios through which liquid–liquid phase separation affects cloud droplet activation and growth are identified and tested in the framework of Köhler theory.

2 Methods

2.1 Technical background

The molecular-scale mechanism of water uptake is studied through the analysis of free-energy profiles. This approach provides a comprehensive overview of the gas-to-particle partitioning process. Molecular simulation methods to calculate free-energy profiles, among them umbrella sampling and steered molecular dynamics, rely on forcing the system to follow a pathway along an aptly chosen set of reaction coordinates that provide a low-dimensional representation of the physical process. In umbrella sampling (Torrie and Valleau, 1977), the reaction coordinate space is mapped on a set of consecutive quasi-equilibrium simulations, with the reaction coordinates restrained at a different value in each simulation. Quasi-equilibrium methods (Sakaguchi and Morita, 2012) provide a free-energy estimate that artificially averages out effects of surface fluctuations (as a result of the method used to average the force as a function of the reaction coordinate) (Darvas et al., 2013; Braga et al., 2016; Klug et al., 2018) whose spatial and temporal scales are similar to those of a typical atmospheric water uptake event.

In steered MD (Park and Schulten, 2004), the system is pulled along the reaction coordinate space with the help of an external harmonic bias at a constant finite velocity or with a constant finite force in several parallel realizations. Jarzynski's equality (Jarzynski, 1997) is used to estimate the free energy from the work profiles collected in each non-equilibrium simulation:

$$e^{-\beta\Delta G} = \langle e^{-\beta W} \rangle, \quad (1)$$

where β is $1/k_B T$ with k_B being the Boltzmann constant and T the temperature. A formal proof of Jarzynski's equality for finite-size systems, coupled to an external heat reservoir (a typical model of a canonical MD simulation), can be found elsewhere (Cuendet, 2006; Schöll-Paschinger and Delgado, 2006). Besides free-energy differences, steered MD can also be used to reconstruct free-energy profiles using different reweighting schemes (Gore et al., 2003). The reweighting is necessary as every “pulling simulation” relies on attaching a harmonic spring to the molecular system in the direction of the reaction coordinate ($s(x, t)$). This signifies adding an external time-dependent bias ($V[s(x, t)]$) to the Hamiltonian ($H_0(x, t)$) of the systems whose coordinates are denoted by x , yielding a perturbed Hamiltonian ($H(x, t) = H_0(x, t) + V[s(x, t)]$), which does not correspond to the unbiased statistical mechanical ensemble in question (Tuckerman, 2010). In this work we use the scheme introduced by Hummer and Szabo (Hummer and Szabo, 2001):

$$e^{-\beta G(s)} = \frac{\sum_t \frac{\langle \delta[s-s(t)] e^{-\beta W_t} \rangle}{\langle e^{-\beta W_t} \rangle}}{\sum_t \frac{e^{-\beta V(s,t)}}{\langle e^{\beta W_t} \rangle}}, \quad (2)$$

where $\langle \dots \rangle$ denotes averaging over parallel realizations.

According to the second law of thermodynamics, it is only possible to provide an upper estimate of the equilibrium free energy related to a process from the work performed, and the equality between work and free energy holds only in the idealized case of transitions that occur at vanishingly small velocities. Equations based on Jarzynski's equality (Gore et al., 2003) can infer free-energy profiles from work profiles accompanying finite-velocity transition. Jarzynski's equality ensures that while the individual trajectories, from which the work along the time-dependent reaction coordinate ($s = s(t)$) is estimated, drive the system out of equilibrium, the free-energy difference is calculated from ensemble averages over the microstates that describe thermodynamic states along the path (Tuckerman, 2010). Thus instead of a single ideal thermodynamically reversible path, the free energy is estimated from a large number of irreversible pathways (that mimic the realistic uptake process) which are weighted according to their distance from the idealized path in the free-energy representation. Jarzynski's equality yields an estimate of the equilibrium free energy regardless of the velocity of the transition, albeit based on a physically realistic set of sample processes.

In practice, Jarzynski's equality and steered molecular dynamics have been successful at examining finite-speed transitions between two states of a molecular system, e.g., protein or nucleic acid unfolding (Park and Schulten, 2004; Gore et al., 2003). The timescale associated with a single water uptake event (impinging plus transport from the surface to the bulk) is ~ 10 ns; surface residence times are ~ 1 ns (Bzdek and Reid, 2017). These timescales are matched by the length of individual realizations in our steered MD simulations. Additionally, initializing each realization (out-of-equilibrium simulation) from different starting configurations (Sect. 2.2) allows impact to happen at any point on the surface, thus incorporating thermodynamically suboptimal pathways – which have a finite probability in experiments – that are well represented in the sample. This approach confers an advantage for estimating the free-energy profile compared to quasi-equilibrium approaches (i.e., umbrella sampling) in which the free energy represents the minimum energy pathway due to the time permitted for sampling the surface. In our systems, finite-velocity pulling allows us to sample transport through humps and wells of the corrugated intrinsic interface (Sect. 3.1.1). These corrugations represent thermodynamically different environments (Bartók-Pártay et al., 2008; Darvas et al., 2010a) for contact formation upon impact and hence different transport pathways which can be relatively far away from the equilibrium one but occur in real events with a finite probability. Note that exploring suboptimal pathways of interfacial mass transfer can be even more important in modeling transport through multicomponent surface films with heterogeneous lateral distributions.

The steered MD method is illustrated in Fig. 1. A sample steered MD trajectory is available as a video supple-

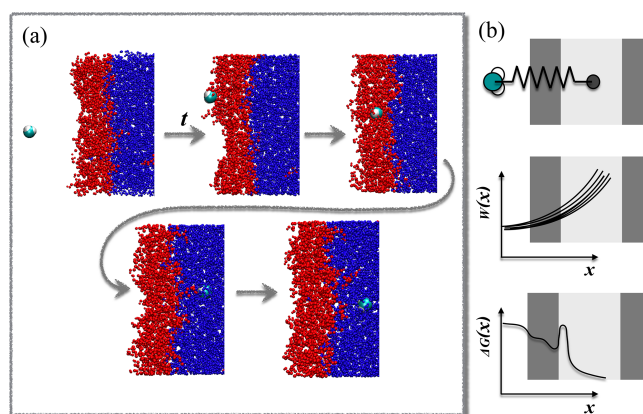


Figure 1. (a) Example of the evolution of a steered MD simulation. (b) Schematic summary of the free-energy reconstruction protocol.

ment (https://zenodo.org/record/4902870#.YLSZwS0Rq_U, last access: 10 September 2021, Lbadaoui-Darvas et al., 2021).

2.2 Simulation details

Steered MD simulations were performed using the GRO-MACS 5.1.3 program package (Abraham et al., 2015). The PLUMED 2.5 plugin (Tribello et al., 2014) was used to implement and control the steered MD simulations. The system consisted of a rectangular slab containing 5000 water molecules enclosed between two multilayers of hydroxycis-pinonic acid (*h*-CPA), each of 125 molecules. The liquid slab was surrounded by a vapor phase from both sides (Fig. 1). The average widths of the layers along the z axis of the simulation box were ~ 6.5 , ~ 2.5 and ~ 6 nm for water, *h*-CPA and the vapor phase, respectively. The protocol to create and equilibrate such interfacial systems is described elsewhere (Hantal et al., 2010; Darvas et al., 2011b). A single water molecule is placed in the vapor phase of the preequilibrated interfacial system and pulled towards the middle of the aqueous phase along the reaction coordinate ($s(x, t)$) – defined as the interface-normal (z) component of the distance connecting its center of mass to that of the aqueous phase by harmonic bias having a force constant of $k = 1000 \text{ kJ mol}^{-1} \text{ nm}^{-1}$. This condition satisfies the stiff-spring approximation which enables the system to closely follow the path of the reaction coordinate by becoming the dominant force in the total dynamics (Hummer and Szabo, 2001) but results in a motion slow enough to mimic diffusive impact. The bias in the reaction coordinate does not constrain the displacement of the pulled molecule in the directions parallel to the macroscopic plane of the interface; thus the impact angle – i.e., the angle between the macroscopic plane of the interface and the vector defined by the initial position of the molecule and its position at the moment of impact – is not constrained to be perpendicular to the surface. These con-

ditions allow us to very closely model realistic atmospheric scenarios in which the impact angle is variable and random. Sample impact angles are shown in Appendix A as snapshot series extracted randomly from three-sample simulations.

A total of 82 parallel 6 ns long realizations are performed at two temperatures, 200 and 300 K, on the *NVT* (canonical) ensemble. This number of simulations is sufficient to provide statistically accurate estimates of the free-energy profiles. Both the standard deviation and the 95 % confidence intervals drop below $0.2 k_B T$ when the number of realizations exceeds 75 (detailed analysis of the statistical accuracy of the simulations is shown in Appendix C). The length of the simulation and the distance covered in the direction of the reaction coordinate result in an average pulling velocity of 1.2 nm ns^{-1} . The realizations differ in the initial position of the gas-phase water molecule in the x,y plane parallel to the surface of the liquid slab and in the random seed which is used to set initial velocity distributions. The choice of pulling velocity is a crucial point in setting up the simulation. It should be low enough to ensure that final and initial states represent the equilibrium distribution (Tuckerman, 2010) and also to yield numerically treatable forces. On the other hand, it has to be large enough to drive the dynamics of the system, and too low transition velocities will undersample higher work pathways. Temperature is kept constant by means of the *V*-rescale thermostat (Bussi et al., 2007). Water molecules are described by the TIP4P water model (Jorgensen et al., 1983) and *h*-CPA molecules by the OPLS force field (Jorgensen and Tirado-Rives, 1988). Alkyl groups are treated as united atoms, while other hydrogens are treated explicitly. Long-range electrostatics are accounted for by the particle mesh Ewald method (Essmann et al., 1995) beyond a cutoff of 1 nm, while Lennard-Jones interactions are smoothly truncated to zero beyond the same cutoff.

3 Results and discussion

Free-energy profiles are interpreted in terms of the local characteristics of the simulated systems, and a detailed mechanism of water uptake is proposed. The decomposition of the free-energy profiles into enthalpic and entropic contributions allows us to identify the thermodynamic drivers of interfacial mass transfer of water at the two studied temperatures. The effect of the complex water uptake mechanism on particle growth and activation is then assessed by estimating interfacial transfer coefficients. Finally, implications for droplet formation are discussed in the light of partitioning timescale estimates, the intraparticle distribution of water within the organic shell and equilibrium saturation ratios.

3.1 Structural and thermodynamic characteristics

3.1.1 Intrinsic density profiles

Local nanoscale fluctuations of fluid interfaces from capillary waves create surface corrugations (Rowlinson, 1982) whose amplitude varies between 0.3 and 1 nm depending on the chemical composition of the surface (Hantal et al., 2010; Darvas et al., 2011a). These corrugations do not average out during typical timescales of the interfacial mass transfer of a water molecule and are enhanced when a molecule crosses the interface (Benjamin, 1993; Karnes and Benjamin, 2016; Benjamin, 2019). Thermal fluctuations are not accounted for by traditional surface definitions and cause artificial smoothing of the surface and systematic errors in the selection of surface molecules (Bartók-Pártay et al., 2008; Jorge et al., 2010). Intrinsic surface analysis – i.e., decoupling surface fluctuations from the interfacial properties (Appendix A) – of molecular simulation trajectories is necessary to resolve the effect of capillary waves on density (Jorge et al., 2010) and free-energy profiles (Darvas et al., 2013; Braga et al., 2016; Klug et al., 2018). Results are sharper and contain features which are smoothed out by fluctuations using traditional surface definitions. The intrinsic surface analysis thus reveals any possible layering near the interface – if the layered structure exists – that is otherwise smoothed out by the smearing effect of the capillary waves. Layering is typically weak in aqueous phases near an organic counterphase. Earlier work reports one pronounced layer and a hardly noticeable second layer for instance in water–dichloroethane systems (Jorge et al., 2010).

In this work, intrinsic analysis is limited to the calculation of density profiles anchored to the fluctuating surface by the ITIM algorithm (Sega et al., 2018), which allows us to establish qualitative connections between the free-energy profiles and the local perturbations in solution structure and thermodynamic properties in the vicinity of interfaces. The algorithm used in this work has the advantage that, instead of defining the covering surface, it selects the molecules of the interface in an exact manner and thus allows for calculating structural and collective properties selectively for the true interface. Repeating this analysis several times consecutively provides sequential molecular layers that can be analyzed separately. This advantage is used for the calculation of the orientational distribution of waters at the surface.

Shaded blue and yellow areas in Fig. 2a and b show the intrinsic mass density profiles of the aqueous and the organic phase. Organic density profiles reveal that the thickness of the organic phase is ~ 1.8 and ~ 2.1 nm at 200 and 300 K, respectively, measured at 5 % of the average height of the profile. It is sufficient to accommodate a disordered double layer but is too low to allow the formation of a bulk phase. The lack of a bulk phase is evidenced by the two neighboring peaks – characteristic of interfaces – in the density profile of the organic phase with no plateau at the bulk-phase

density (1.2 g cm^{-3}) in between. The layer-by-layer density profiles obtained from the ITIM algorithm lead to the same conclusion (Appendix A). A $\sim 85\%$ local drop in the total density (sum of water and organic density) compared to that of the bulk aqueous phase can be observed at the Gibbs dividing surface of the two condensed phases at both temperatures. The affected region is wider at 300 K. The interface in our systems is mixed, and the density drop results from the presence of voids larger than the typical distances between the molecules in the bulk. A more detailed analysis of the interface structure and a demonstration of the voids are found in Appendix A. The interfacial region is characterized by an overlap between the organic and the water density profiles which is due to partial miscibility of the two phases. The width of this mixed region is 1.5 nm at 300 K and 1.2 nm at 200 K disregarding the small peak of organics in the bulk aqueous phase. The aqueous phase has two consecutive peaks characteristic of the first two molecular layers, followed by a bulk-phase plateau. The second peak is less pronounced than the first, and the shape of the profile is consistent with previous results (Bresme et al., 2008; Jorge et al., 2010). The enhanced structure in the intrinsic density profile of water compared to the global profiles is shown in Appendix A. The interface and subsurface structure are similar but more pronounced at 200 K as a result of reduced thermal motion which preserves layered structure at low temperatures.

3.1.2 Free-energy profiles

Helmholtz free-energy profiles, which represent the thermodynamic state function in the canonical ensemble, are calculated. While the Helmholtz free energy is formally different from the experimentally determined Gibbs free energy, in systems containing incompressible condensed phases the additional $p\Delta V$ term is negligibly small; thus the two quantities can be assumed to be the same within a small error. Free-energy profiles with the reference state assigned to the bulk aqueous phase are overlapped with the intrinsic mass density profiles in Fig. 2a and b. Profiles are significantly different at the two temperatures, which suggests that the mechanism of gas-to-particle partitioning in LLPS particles is temperature dependent. Despite differences, simulations show two common characteristics: (i) the negative free-energy difference (ca. $-19.5 \text{ kJ mol}^{-1}$ at 300 K and ca. $-29.0 \text{ kJ mol}^{-1}$ at 200 K) between the bulk aqueous and the vapor phase, which underlines that overall water uptake from the vapor phase is thermodynamically favored, and (ii) the lack of a free-energy barrier at the vapor–organic interface, which is the main difference between free-energy profiles of transfer through hydrophobic media, for which large maxima have been observed leading to reduced surface accommodation coefficients (Sakaguchi and Morita, 2012; Ergin and Takahama, 2016). The free-energy differences between the liquid and the vapor phase agree within 25 % and 9 % with the

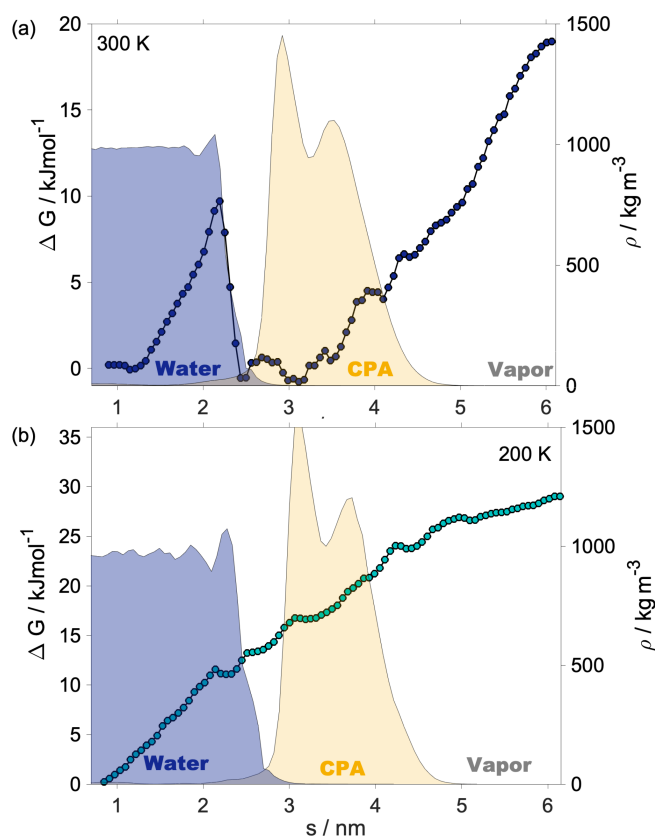


Figure 2. (a) Free-energy and density profiles at $T = 300 \text{ K}$; (b) the same profiles at $T = 200 \text{ K}$.

data estimated from experimental densities and vapor pressures at 300 and 200 K, respectively. Temperature-dependent trends are consistent with expectations; however, the simulations only reproduce experimental thermodynamic data semi-quantitatively, which can be attributed to the accuracy of transferable potentials combined with the complexity of the studied system. A detailed description of the comparison can be found in Appendix C.

The free-energy profile at 300 K begins with a plateau characteristic of the vapor phase, followed by a steep decrease ($\sim 5 \text{ kJ mol}^{-1}$) at the vapor–organic interface. A monotonic decrease in the free-energy profile characterizes the transfer of the water molecule in the organic phase. The lack of a plateau is related to the fact that the organic layer is not thick enough to accommodate a bulk phase, which results in a position-dependent anisotropy caused by the proximity of both interfaces in combination with the partial dissolution of the water in the organic phase, evidenced by non-zero water density of up to $|s| \approx 3.5 \text{ nm}$. The presence of dissolved water molecules results in the near-0 free energies in the inner half of the organic phase and a small maximum (0.6 kJ mol^{-1}), considerably smaller than the energy of thermal motion ($3/2k_B T$), which is thus considered statistically insignificant but which can however be poten-

tially associated with the increased order in the first molecular layer in the organic phase. The free-energy profile has a local minimum at the organic–water interface and a maximum ($\sim 9.8 \text{ kJ mol}^{-1}$) corresponding to the first molecular layer of water, seen as a peak in the intrinsic density profile, beyond which the profile smoothly decreases to the reference state value in the bulk aqueous phase. The free-energy profile at 200 K is considerably smoother: the magnitude of none of the features exceeds the energy of thermal motion ($3/2k_{\text{B}}T$) at the corresponding temperature; thus any small local minimum or maximum can be viewed as statistically insignificant. The minimum and the peak at the organic–water interface characteristic of the room temperature profile cannot be observed at low temperature. While vapor-to-organic transfer is a favorable and barrierless transition at both temperatures, the transport between the organic shell and the core is hindered by the presence of the free-energy barrier at 300 K, which diminishes at low temperature. We acknowledge that the profiles assume a somewhat unusual shape in the region where they decay to the bulk-aqueous-phase value and attribute this to the large mutual solubility of the two phases which results in an extended region where both water and *h*-CPA molecules are found at varying concentrations. Large temperature-induced differences suggest that the thermodynamic driving forces are strongly temperature dependent. One possible explanation is that they are of entropic nature, and their strength is explicitly scaled by the temperature through the $-T\Delta S$ term.

3.1.3 Internal energy profiles and entropy

To test the hypothesis that features of the free-energy profile are of entropic origin, internal energy profiles are calculated and shown in Fig. 3. The sum of the interaction energies of the pulled water with the surrounding molecules is used as a surrogate for the internal energy; the calculation is described in detail in Appendix B. In principle, the total entropy profile can be obtained trivially by subtracting the internal energy profile from the free-energy profile; however given that neither the free-energy profiles nor the internal energy profiles can be assumed to be quantitative, the physical significance of their difference is questionable; hence total entropy profiles are not shown here. Instead, distinct entropy contributions are analyzed in detail, which have been selected to explain the features of the free-energy profiles.

Internal energy profiles in Fig. 3a show that water uptake is energetically favorable, the difference between the pulled water molecule being in the vapor phase and in the aqueous phase is ca. -55 kJ mol^{-1} at 300 K and ca. -60 kJ mol^{-1} at 200 K. Internal energy differences correspond approximately to the formation of three to four hydrogen bonds by the pulled molecule if the average energy of a hydrogen bond is assumed to be $15\text{--}20 \text{ kJ mol}^{-1}$ (Wendler et al., 2010), which is also supported by the hydrogen bond profile calculated for a randomly selected realization (Appendix A). Internal en-

ergy profiles are smooth and show a similar overall behavior at the two temperatures. A small drop in the internal energy whose magnitude is ~ 3 and $\sim 5 \text{ kJ mol}^{-1}$ at 200 and 300 K, respectively, indicates the formation of contact with the organic phase. It is however not sufficiently low compared to the internal energy observed in the subsequent bulk organic phase to energetically stabilize a surface-adsorbed state. Both internal energy profiles have a plateau spanning the outer half of the organic phase, where water molecules from the bulk aqueous phase do not penetrate. This is followed by a smoothly decreasing part which corresponds to the pulled molecule forming an increasing number of hydrogen bonds with both *h*-CPA and the water molecules dissolved in the organic phase. Near the organic–water interface and in the aqueous phase, the internal energy profiles are close to identical at the two temperatures, suggesting that specific features of the free-energy profile are of entropic origin.

Configurational entropy profiles calculated using Schlitter's formula (Baron et al., 2006) as explained in Appendix B are close to constant throughout the condensed phase: $-T\Delta S_{\text{config}}$ is 25 kJ mol^{-1} at 300 K and 14 kJ mol^{-1} at 200 K. They are thus not responsible for any of the features in the free-energy profiles. Interfacial entropy ($T\Delta S_{\text{IF}}$) at the vapor–organic interface is approximately 5 kJ mol^{-1} at 300 K and is negligibly small at 200 K (Appendix B). Despite the positive value of interfacial entropy the overall entropy, difference between the vapor and the organic phase is a small negative value, which – together with the moderate change in enthalpy at the interface – is responsible for the lack of surface-adsorbed states. A possible explanation for the overall negative entropy is the ordering of the organic molecules at the surface which reduces orientational degrees of freedom in a similar manner to that described later for the water–organic interface.

Conformational entropy profiles, calculated from the mole fraction profiles of the water and the organic molecules (Appendix B), are shown in Fig. 3c. They exhibit a peak located at the organic–water interface at both temperatures and are close to zero elsewhere. These peaks represent the effect of non-ideal local mixing of two phases in this region. The conformational entropy peak is slightly higher at 300 K, mostly due to the higher temperature. This and the local $\sim 85\%$ decrease in the total density in this region explain the presence of the free-energy minimum at the organic–water interface. Lower density ensures the reduction in steric hindrance for any conformations without losing hydrogen bonds. The combination of the two above-described effects explains the minimum in the free-energy profile observed at the water–organic interface at 300 K. High conformational degrees of freedom manifest in subsequent detaching/attaching of the pulled molecule between the organic and aqueous phase in varying orientations, which can be observed only in the 300 K simulations (video supplement available). The conformational entropy profile peak in the interfacial region is significantly ($\sim 40\%$) smaller at 200 K. Additionally, the low-

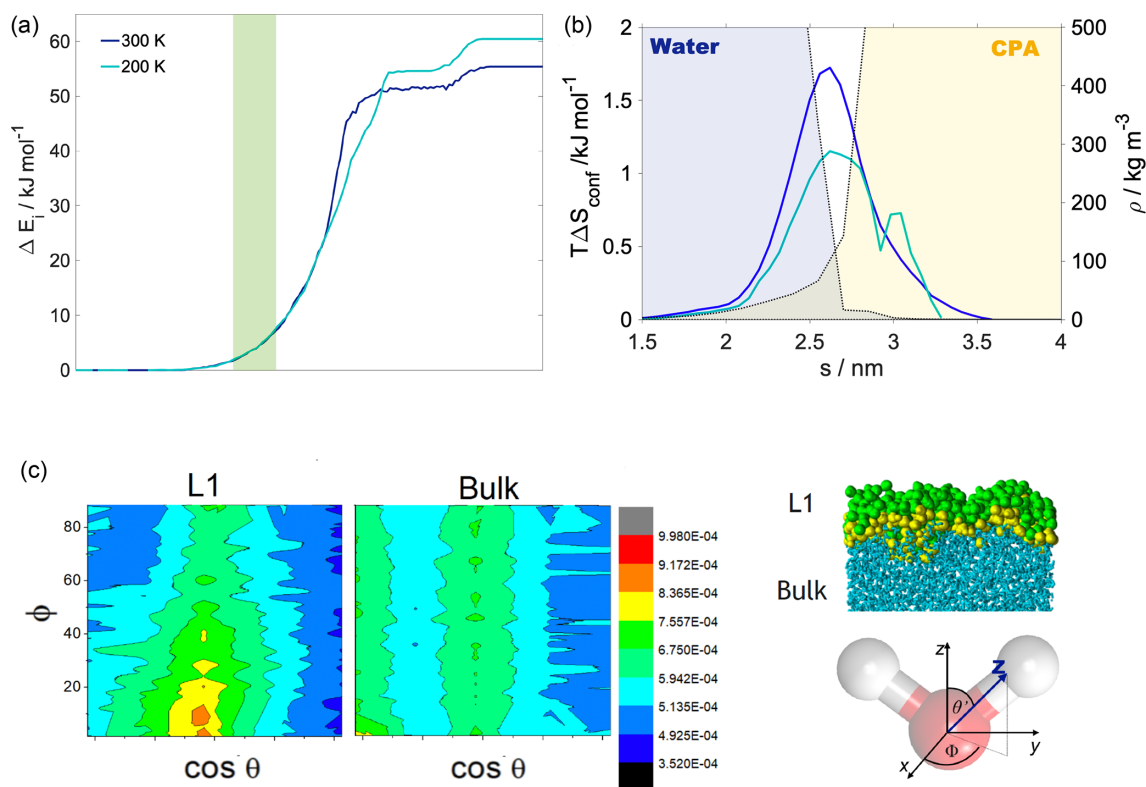


Figure 3. (a) Internal energy profiles. (b) The conformational entropy in the interfacial region overlapped with intrinsic density profiles of the aqueous (blue-shaded) and the organic (yellow-shaded) phase. (c) Left: orientational maps of the water molecules in the first molecular layer (L1) of the aqueous phase and in a randomly selected layer in the bulk phase. Right: an equilibrium snapshot from a simulation showing the first two molecular layers (green and yellow balls) and the bulk phase (cyan sticks) as determined by the ITIM algorithm; the definition of the orientational vectors of the water molecule.

density region is narrower due to the pronounced shoulder in the water density profile (Fig. 2); thus steric effects are not as effectively reduced as at 300 K. The joint decrease in the magnitude of both contributions leads to the disappearance of the free-energy minimum at the organic–water interface at 200 K.

The increased orientational order of molecules at interfaces of molecular liquids locally reduces orientational entropy, which is responsible for the free-energy peak coinciding with the first two molecular layers of water in the 300 K simulations. Interfacial molecules adapt preferred orientations owing to topological anisotropy of intermolecular interactions, in contrast to the bulk where the close-to-isotropic energetic environment ensures nearly random orientations. To illustrate the differences between the orientational preferences of interfacial and bulk water molecules, we calculate the joint distribution of the two angles defined in the bottom right panel of Fig. 3c in the first molecular layer and in a randomly selected molecular layer from the bulk aqueous phase. Details of the calculation are summarized in Appendix B. The two dimensional joint distribution of these two angles (Fig. 3c, top panel) is able to define the orientation of a rigid body having a C_{2v} point group symmetry with respect

to an external axis. The peak shows that in the first layer water molecules tend to lie parallel to the surface, whereas the bulk-phase distribution shows no significant preferences. Increased orientational order results in a decrease in orientational entropy, corresponding to the maximum of the free-energy profile. The second layer of water has similar orientational preferences (Appendix B), which explains the shoulder of the free-energy profile near the second molecular layer. Similar results are found for 200 K (Appendix B); thus the observed temperature dependence results again from the explicit scaling of the importance of entropy with temperature. Orientational entropies are also estimated in one dimension (Appendix B), but due to symmetry reasons they do not give a quantitative description of the ensemble of ordering effects.

3.1.4 Generalization of the driving forces

The question of whether the thermodynamic driving forces identified in the previous section are system specific or generalizable over a wider range of compositions that can yield LLPS particles is important for determining the level of confidence with which implications for atmospheric aerosol can be stated based on these simulations. The most prominent

characteristics of the free-energy profiles are (i) the lack of a minimum at the vapor–organic interface, (ii) the minimum at the organic–water interface and (iii) the maximum corresponding to the first layer of the aqueous phase.

Experimental and molecular simulation studies show that driving forces which lead to the appearance of these features are generally present in interfacial systems involving molecular liquids or solids. (i) The value of the free energy at the vapor–organic interface is moderated by the increased order of organic molecules which has been observed from experiments and simulations in pure water (Cipcigan et al., 2015) and pure organics (Darvas et al., 2010a) as well as in concentrated (Darvas et al., 2010b) and dilute aqueous organic solutions (Takamuku et al., 1998; Pártay et al., 2008; Pojžák et al., 2010; Ghatee et al., 2011; Makowski et al., 2016). (ii) The density drop in the interfacial region and the enhanced local mixing which invoke the free-energy minimum at the organic–water interface at 300 K are characteristic of any liquid–liquid interface (Fernandes et al., 1999; Jedlovsky et al., 2002; Hantal et al., 2010; Jorge et al., 2010; Darvas et al., 2011b, 2013). The extent of local mixing is a non-trivial function of the hydrophilicity of the organic compound and the types of intermolecular interactions. (iii) Orientational preferences of water molecules near liquid–liquid or liquid–solid interfaces, which account for the maximum of the free-energy profiles, are also generally present in interfacial systems. They have been observed in molecular simulations several times at various liquid–liquid interfaces such as carbon tetrachloride–water (Hantal et al., 2010; Kertész et al., 2014) or dichloroethane–water (Hantal et al., 2010) and have been proved to be enhanced next to a solid counter-phase (Kertész et al., 2014).

The strong temperature dependence follows directly from the entropic nature of these driving forces and the definition of the free energy. Consequently, besides the presence of the driving forces, their temperature dependence is also expected to be generally valid. Liquid–liquid phase separation is known to form if $O : C < 0.8$, the organic components in the examples listed above cover the complete $O : C$ ratio range. Thus our findings are likely not system specific and represent a typical behavior for sparingly soluble organic compounds present in the atmosphere, although exact values of the thermodynamic quantities can vary from system to system. The following implications are thus quantitatively only valid for the water–*h*-CPA–vapor system, while qualitatively similar behavior can be expected for a wider variety of liquid–liquid phase separation forming cases.

3.2 Implications for water uptake and particle growth kinetics

3.2.1 Atmospheric relevance of the simulated systems

The simulations presented in this paper aim to provide a qualitative description of how the change in temperature af-

fects the mechanism of water uptake in a particle formed at a lower height (higher temperature) while rising. LLPS particles formed at lower altitudes will likely preserve the phase-separated structure also at high altitudes; therefore the same system structure is used at both temperatures.

The first temperature is chosen to represent conditions near the boundary layer or standard laboratory conditions. At 300 K the particles are trivially in the liquid state, and the $O : C$ ratio of 0.4 of *h*-CPA suggests that liquid–liquid phase separation is a realistic assumption (Song et al., 2012). The temperature of 200 K is chosen to model conditions in the upper troposphere. We acknowledge that this is an extremely low temperature to examine; however it is common in molecular simulations to use exaggerated conditions in order to accentuate trends along variables such as temperature or pressure, e.g., Darvas et al. (2012). As seen in the previous section the structure of the aqueous phase is more pronounced at 200 K than at 300 K; however the observed density profiles are very different from those of crystalline ice, which is consistent with the difficulty of producing crystalline ice spontaneously from atomistic simulations (Matsumoto et al., 2002). The phase state of the system at 200 K is inferred from the diffusivity of water, which is calculated from three randomly selected trajectories using the Einstein equation (Einstein, 1905). The obtained average value of $D \sim 10^{-13} \text{ m}^2 \text{ s}^{-1}$ suggests our system is in a semisolid state. The glass transition temperature of pure *h*-CPA inferred from its molecular weight and $O : C$ ratio (Shiraiwa et al., 2017) is approximately 190–210 K. This together with the low $O : C$ ratio suggests that similar particles would be phase separated and either glassy or semisolid. A recent study shows that semisolid liquid–liquid phase separation comprises the dominant phase state of SOA in the upper troposphere (Schmedding et al., 2020). Hence, despite the exaggerated temperature, our system is a valid model of a typical SOA particle in the upper troposphere.

The simulated systems consist of a macroscopically flat model of an LLPS particle. The flat-surface approximation is a generally accepted model of larger particles, where the surface curvature can be neglected. For instance, for aqueous particles mass accommodation coefficients on the planar surface become equal to those estimated for spherical particles beyond particle diameters on the order of 20–30 nm (Barclay and Lukes, 2019). We stress once again that, for reasons described in the Methods section, impact angles are not limited to 90° and are randomly selected by the thermal motion of the particle in the vapor phase; thus our model closely mimics realistic gas–particle collisions.

3.2.2 Interfacial transfer coefficients

Interfacial transfer coefficients are estimated from the activation free energies characteristic of the vapor-to-organic ($k_{v/o}$) and organic-to-water ($k_{o/w}$) transfer using the transition state

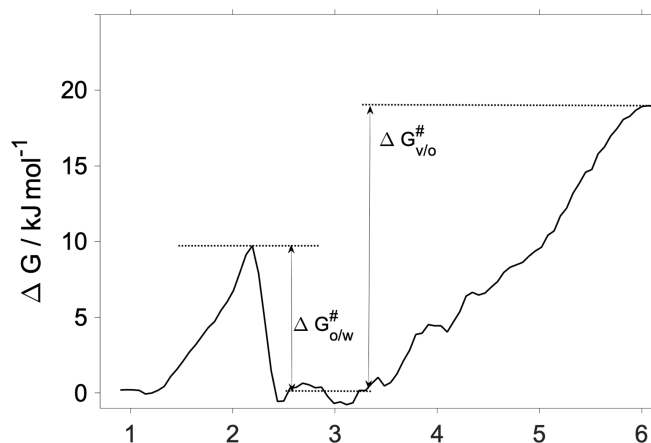


Figure 4. Definition of activation free energies at the different interfaces at $T = 300$ K.

theory as

$$k_{i/j} = \exp \left[\frac{-\Delta_{ij}^{\ddagger} G}{RT} \right], \quad (3)$$

where i and j indicate the phases forming the interface in question. The corresponding activation free energies are illustrated using the 300 K free-energy profile in Fig. 4. While the transfer coefficient calculated here is conceptually different from the mass accommodation coefficient used in atmospheric applications, chemical kinetic frameworks are widely used to estimate α from free-energy profiles (Grote and Hynes, 1980; Taylor and Garrett, 1999; Truhlar and Garrett, 2000; Sakaguchi and Morita, 2012; Ergin and Takahama, 2016). We note that due to the lack of a well-defined bulk-phase plateau in the organic phase, we choose an average free energy characteristic of the middle of the organic phase as a reference value (0.6 kJ mol^{-1}). This choice is arbitrary, and a different definition may slightly modify obtained transfer coefficients, albeit without significantly altering values, trends and conclusions. Vapor-to-organic (surface) transfer coefficients ($k_{v/o}$) are near unity at both temperatures, whereas organic-to-water (core) transport is characterized by $k_{o/w} = 0.03$ at 300 K and $k_{o/w} = 1$ at 200 K.

The vapor-to-organic transfer coefficients resemble most closely the commonly used definition of the mass accommodation coefficient, which considers either adsorption at the surface or absorption in the first few molecular layers of the particle phase as the final state of gas-to-particle partitioning. Due to the lack of maxima or minima at the vapor–organic interface, in our systems surface-adsorbed states of the water are thermodynamically indistinguishable from those with the water absorbed by the subsurface region.

The organic-to-water transfer coefficient ($k_{o/w}$) is reduced compared to the mass accommodation coefficients ($k_{v/o}$) at room temperature owing to the free-energy barrier corresponding to the first molecular layer of water. As opposed to

mass accommodation coefficients which show no temperature dependence, $k_{o/w}$ follows a similar trend with temperature to that observed for water uptake on a hexadecanol monolayer (Davies et al., 2013) and on pure water (Davidovits et al., 2004). The fact that core uptake coefficients differ significantly from mass accommodation coefficients highlights the possibility that the traditional representation of water uptake by a single value of α or an effective uptake coefficient may have to be complemented by a temperature-dependent core uptake term to fully describe water uptake by phase-separated aerosol.

3.2.3 Mass accommodation coefficients

Mass accommodation coefficients defined by vapor-to-organic transfer coefficients are near unity and agree well with the globally representative values proposed in modeling studies (Raatikainen et al., 2013), as well as with recent experiments which report large mass accommodation coefficients (Liu et al., 2019) and unhindered gas-to-particle partitioning of water and organics in phase-separated particles (Gorkowski et al., 2017). While global datasets of CCN concentrations can usually be described by $0.1 < \alpha < 1$, implying uninhibited water uptake (Raatikainen et al., 2013), compressed hydrophobic organic films can result in mass accommodation coefficients as low as 0.001. In such systems, α is correlated with the integrated carbon number density (Ergin and Takahama, 2016) of the organic layer, estimated as the integral of the density profile along the outer half of the organic layer divided by its width. The integrated carbon number density for our systems is 14 nm^{-3} which for a completely hydrophobic film comprised solely of aliphatic CH moieties would correspond to $\alpha \sim 0.01$ (Ergin and Takahama, 2016) instead of the observed near-unity values. In the presence of hydrophilic functional groups – which form hydrogen bonds and dipole–dipole interactions – such a simple descriptor is insufficient to reliably predict mass accommodation coefficients.

Reduction in mass accommodation coefficients results in increased CCN number concentrations. The explanation for this effect is that droplet number concentrations in ambient clouds depend on the maximum supersaturation, S_{max} , which is largely determined by the condensation rate of water vapor on the growing droplets. Reduced α values correspond to low water vapor condensation rates – which allow supersaturation to develop for longer periods of time (compared to when α is larger), resulting in increased S_{max} and droplet concentrations. Model simulations predict a mild 1.2-fold increase in CCN number concentrations for $\alpha = 0.1$, a 1.5- to 1.8-fold increase for $\alpha = 0.01$ and a 2- to 2.5-fold increase for $\alpha = 0.001$ (Raatikainen et al., 2013). In this framework, near-unity mass accommodation coefficients obtained from our simulations at both temperatures are not expected to alter droplet number concentrations, further supporting the asser-

tion that kinetic delays do not explain the increased CCN activity of LLPS aerosol.

3.2.4 Core uptake coefficients

The hindered mass transfer of water between the organic shell and aqueous core together with the uninhibited mass accommodation of water in LLPS aerosol results in different condensational growth rates of the core and shell, leading to a dynamic retention of water by the organic shell. We use the $k_{v/o}/k_{o/w}$ ratio to estimate the extent of the dynamic retention of water by the organic phase. The value is approximately unity at 200 K and about 30 at 300 K. The growth rate of the organic shell is thus substantially larger at 300 K than that of the core, which is in agreement with results of multilayer kinetic model (KM-GAP) calculations which also evidence faster condensational growth of the particle shell than of the core (Shiraiwa et al., 2013). This suggests that the aqueous core contains less water and the organic shell is more dilute at any time during growth of the particle than predicted assuming that mass transfer kinetics can be described by a single α value.

Retention of water in the organic shell due to the reduced core uptake coefficient (organic-to-water or vapor-to-water transfer coefficient) may affect equilibrium properties (vapor pressure and surface tension) which determine cloud droplet growth and activation. Increased water content of the organic shell can increase vapor pressure and surface tension, which both affect cloud droplet growth. In the extreme case, inhibited transport between the shell and the core, indicated by reduced core uptake coefficients, may invoke swelling and – depending of the solubility of the organic compounds – dissolution of the shell. These hypotheses can be relevant if the vapor phase is in dynamic equilibrium with the organic shell containing an increased amount of water and this equilibrium is unaffected by the presence of the aqueous core; in other words water uptake happens only by the shell. For this condition to hold, the gas-to-particle partitioning timescale of water (τ_s) should be significantly shorter than the timescale of transfer from the shell to the core (τ_c). Timescales are estimated as the e -folding times of condensation–evaporation, assuming that both gas-to-particle and shell-to-core partitioning can be described as in Saleh et al. (2013):

$$\tau = \frac{1}{2\pi D F d N}, \quad (4)$$

where $F = (1 + Kn)/(1 + 0.3773 Kn + 1.33 Kn(1 + Kn)/\alpha)$ is the Fuchs–Sutugin correction factor, with Kn being the Knudsen number and α the transfer coefficient of the given process. For gas-to-particle partitioning Kn is 10^{-2} , 10^{-1} and 10^0 ; α is 1; the gas-phase diffusion coefficient of water is estimated at 0.26 and $0.128 \text{ cm}^2 \text{ s}^{-1}$ at 300 and 200 K (Pruppacher and Klett, 2010); and d is the diameter of the particle (100 nm). For core-to-shell partitioning Kn is approximated as the ratio of the diameter of the h -CPA molecules

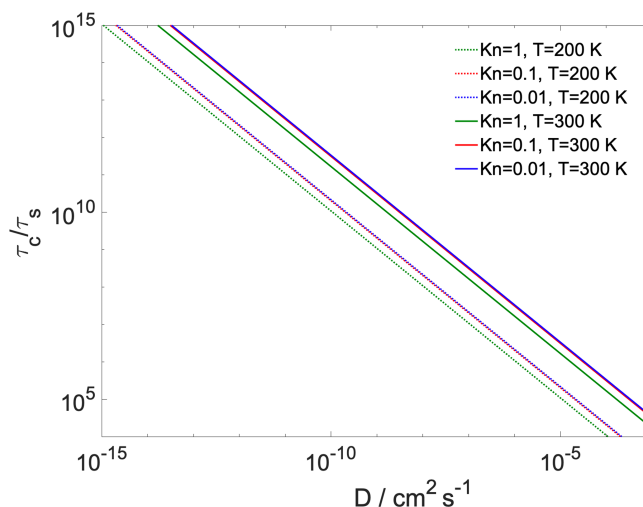


Figure 5. The ratio of characteristic timescales of shell-to-core and gas-to-particle partitioning as a function of bulk-phase diffusivity of the water in the organic shell at varying gas-phase Knudsen numbers and temperature. At 300 K model calculations are presented using both the lower and the upper of the core uptake coefficient.

and the width of the organic layer, α is $k_{o/w}$, d is the core diameter, and the diffusion coefficient (D) is varied between 10^{-3} and $10^{-9} \text{ cm}^2 \text{ s}^{-1}$. The ratio between the core and the full particle diameter is the same as the ratio of the width of the organic shell and the total system width. Assuming the particle number concentration (N) to be 1000 cm^{-3} , the equilibration timescale of gas-to-particle partitioning τ_s is on the order of 1–2 min, which is similar to timescales reported for the equilibration of semivolatile molecules (Saleh et al., 2013). $\tau_c/\tau_s > 10^3$ in every case (Fig. 5); thus the hypothesis of equilibrium between the organic shell and the vapor phase holds for our system at both temperatures and the water uptake by the particle core is somewhat hindered. The ratio of the timescales is at least 3 orders of magnitude even when the core and shell uptake coefficients are assumed to both be unity (200 K), owing to the difference between gas- and particle-phase diffusivity. Reduced core uptake coefficients further increase this difference by orders of magnitude. In summary, as expected, the equilibration timescale of gas-to-particle partitioning is sufficiently short to assume equilibrium between the vapor phase and the organic shell, while core uptake may not reach equilibrium within a typical model of cloud updraft.

3.2.5 The effect of bulk diffusion and non-uniform concentration distribution

The non-negligible free-energy difference between the vapor–organic and the organic–water interface potentially alters the above-described uniform increase in the water concentration in the shell and carries consequences for droplet growth and activation. A more detailed understanding of

these effects can be obtained by converting the free-energy profile using the expression $\Delta G(s) = -k_B T \ln c_{\text{rel}}(s)$ into a probabilistic density profile $c_{\text{rel}}(s)$, which corresponds to an equilibrium concentration profile of the condensing water in the organic phase at arbitrary values of the vapor pressure. This equilibrium concentration profile is calculated under the assumption of instantaneous diffusion and bears no information about the surrounding relative humidity (RH) and is valid for a mostly organic shell (as the free-energy profiles were derived for pulling simulations of single water molecules). The effect of the non-instantaneous bulk-phase diffusion of water and RH are accounted for by a correction factor, f :

$$c_{\text{rel}}(s) = \exp \left[\frac{-\Delta G(s)}{k_B T} \right] f(D_p, C_v); f(D_p, C_v) = \frac{1}{1 + \frac{\alpha \omega C_v}{4 D_p \rho_p}} \quad (5)$$

C_v and D_p are the vapor-phase concentration of water and the bulk-phase diffusion coefficient of water in the organic phase, respectively; ω is the mean thermal velocity of water in the vapor phase; α is the mass accommodation coefficient, and ρ_p is the density of the organic phase (1.2 g cm^{-3} in our calculation). The correction factor was adapted from Shiraiwa and Pöschl (2020), who derived an expression to account for the effect of diffusivity on gas-to-particle partitioning by introducing a penetration-depth-dependent definition of the mass accommodation coefficients of organic molecules absorbed by aerosol particles used in particle growth kinetic models (Shiraiwa et al., 2012). Our model calculations are performed at five RH values in the range of 50%–98%, using 13 different diffusion coefficients between 10^{-15} and $10^{-3} \text{ cm}^2 \text{ s}^{-1}$, characteristic of liquid and semisolid particles. $c_{\text{rel}}(s)$ is normalized to the 0–1 range, with 0 and 1 corresponding to the minimum and maximum of the $c_{\text{rel}}(s)$ profile within the organic phase at 300 K.

Figure 6 shows the diffusion-corrected equilibrium concentration profiles at RH = 95% at 300 K (panel a) and at 200 K (panel b). Condensing water molecules show a strong preference to be accommodated near the organic–water interface, while the vicinity of the vapor–organic interface is depleted in water at 300 K (Fig. 6a) for bulk-phase diffusion coefficient values characteristic of the liquid phase ($10^{-3} < D_p < 10^{-9} \text{ cm}^2 \text{ s}^{-1}$). A much less pronounced concentration gradient, about an order of magnitude smaller than that found at room temperature, can be observed at 200 K if liquid-phase diffusivities are assumed. The effect of diffusion is negligible in the $10^{-3} < D_p < 10^{-6} \text{ cm}^2 \text{ s}^{-1}$ diffusivity range. The steepness of the concentration gradient is reduced by 40% and 85% for $D_p = 10^{-7}$ and $D_p = 10^{-8} \text{ cm}^2 \text{ s}^{-1}$ at 300 K and by 30% and 82% for $D_p = 10^{-8}$ and $D_p = 10^{-9} \text{ cm}^2 \text{ s}^{-1}$ at 200 K. Slow diffusion in highly viscous liquid and semisolid states ($D_p < 10^{-10} \text{ cm}^2 \text{ s}^{-1}$) cancels out the effect of thermodynamic preferences and results in uni-

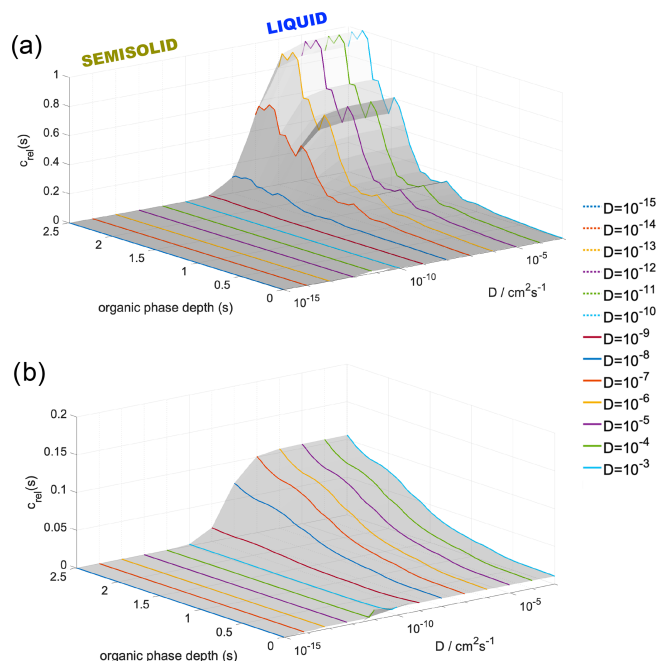


Figure 6. Modeled, diffusivity-corrected concentration gradient of water in the organic phase at (a) 300 and (b) 200 K at 98% RH and at varying diffusion coefficients. Organic-phase depth describes the distance from the vapor–organic interface; zero corresponds to the Gibbs dividing surface between the vapor and particle phase.

form concentration profiles at both temperatures. Concentration profiles are not sensitive to varying RH; thus only one characteristic example is shown in Fig. 6. Water's diffusion coefficient in *h*-CPA is estimated from separate unpublished MD simulations to be 10^{-5} to $10^{-6} \text{ cm}^2 \text{ s}^{-1}$ at 300 K depending on concentration and 10^{-7} to $10^{-8} \text{ cm}^2 \text{ s}^{-1}$ at the lower temperature; similar values have also been reported based on experiments (Lienhard et al., 2015). This means that room temperature concentration profiles are virtually unaffected by bulk-phase diffusion as liquid-like diffusivities apply. Diffusion control is only probable for diffusion coefficients characteristic in semisolid particles. At 200 K, the originally small concentration gradient is further reduced by slow diffusion. Bulk-phase diffusion becomes the governing process for water uptake at low temperatures, regardless of the assumed value of the diffusion coefficient.

The quantitative description is only valid for the system studied and magnitudes may vary as a function of the composition of the organic shell. However, like the main driving forces of the water uptake process, the formation of the concentration gradient can be expected in generic LLPS particles regardless of their actual chemical composition. The shape of the concentration profiles may change for a thicker organic layer having a bulk phase corresponding to a constant plateau in the free-energy profile, which converts into a constant concentration region in the middle of the organic phase. Nevertheless, the maximum of the concentration profile coincides

with the minimum of the free-energy profile at the organic–water interface, which is determined predominantly by local entropy increase due to the lower density and increased conformational degrees of freedom, which is universal at boundaries between condensed phases. Similar considerations are valid for the minimum of the concentration profile, which is observed at the vapor–organic interface, whose value mainly depends on an interplay between intermolecular interactions, the orientational order of the vapor–organic interface and interfacial entropy, which are largely insensitive to the thickness of the organic phase. The significant enrichment of the water–organic interfacial region in water may lead to a local dissolution of the organic phase. However, even when dissolution of the organic phase occurs, the strong preference of water molecules to be accommodated in the inner part of the organic shell results in depleted water concentrations at the surface, which ensures the presence of an organic rich film at the surface and hence maintains low surface tensions despite the elevated water concentration in the organic shell even when relative humidity approaches 100 %. This is consistent with recent experiments and model calculations which conclude that liquid–liquid phase separation persists up to very high relative humidities (Liu et al., 2018).

3.2.6 Equilibrium saturation ratios

The dynamics of water uptake affects the composition profile within the particle and hence the equilibrium vapor pressure of water over its evolution. For instance, kinetic hindrance of water molecules moving between the organic shell and aqueous core will lead to a higher water content in the outer shell than one in which such hindrances do not exist. Concentration profiles of water within the shell affect the water mole fraction and also droplet surface tension. Based on the findings from previous sections, three distinct scenarios through which liquid–liquid phase separation may affect equilibrium saturation ratios of water are considered (Table 1). Given a fixed mass of dry substance, we use Köhler theory to calculate differences in equilibrium saturation ratios based on these assumptions of how the driving force for water vapor condensation may be affected by chemical distribution and transport dynamics within an individual particle.

Scenario (i) is valid at 300 K until the overall water concentration in the shell becomes too large for the gradient to prevent the formation of a well-mixed aqueous layer at the surface. Scenario (ii) is a model of the 200 K behavior as well as that of 300 K from the point where the concentration gradient cannot prevent the presence of a non-negligible amount of water in the surface layer. Scenario (iii) is a hypothetical case that provides a lower bound on the water content in the shell. Scenario (iv) provides a base case where the distribution of species is considered to be homogeneous throughout the particle.

- i. Liquid–liquid phase separation is present; core growth is kinetically hindered, and the concentration gradient

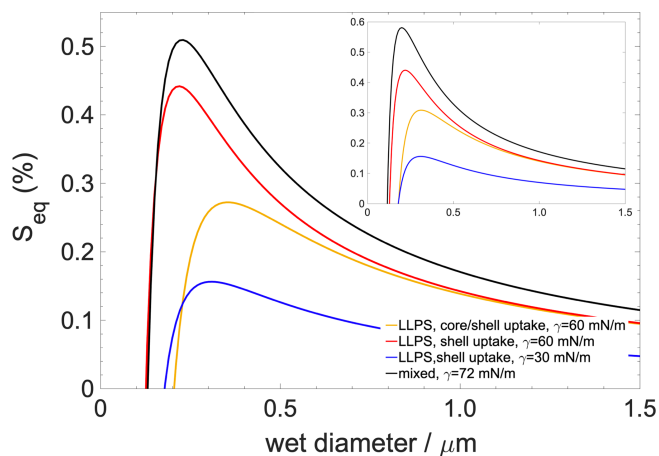


Figure 7. Köhler curves for a 50 nm dry-diameter particle containing 90 % organics with 10 % salt ((NH₄)₂SO₄). The inset shows Köhler curves for a dry particle which contains organics only. Black curve: well-mixed case; blue curve: scenario 1 (hindered core uptake with concentration gradient); red curve: scenario 2 (hindered core uptake without concentration gradient); yellow curve: scenario 3 (unhindered core uptake without concentration gradient).

of the water in the organic shell is such that a nearly pure organic layer can be assumed to cover the particle surface. This is a valid model at 300 K until the overall water concentration in the shell becomes too large for the gradient to prevent the formation of a mixed aqueous layer at the surface. Surface tension is characteristic of that of the pure *cis*-pinonic acid: $\gamma = 30 \text{ mN m}^{-1}$ (Hyvärinen et al., 2006).

- ii. Liquid–liquid phase separation is present; core growth is kinetically hindered, but the lack of the concentration gradient results in a mixed surface layer whose surface tension is set to be equal to that of an aqueous *h*-CPA solution at the solubility limit: $\gamma = 60 \text{ mN m}^{-1}$ (Hyvärinen et al., 2006). This scenario is a model of the 200 K behavior as well as that of 300 K from the point where the concentration gradient cannot prevent the presence of a non-negligible amount of water in the surface layer.
- iii. Liquid–liquid phase separation is present, but the effect of kinetic hindrance of core uptake is ignored. This is a hypothetical case; the surface tension is characteristic of the saturated mixture of water and *cis*-pinonic acid: $\gamma = 60 \text{ mN m}^{-1}$ (Hyvärinen et al., 2006).

Köhler curves are calculated for particles having a 50 nm dry diameter consisting of 90 % organic compounds and 10 % ((NH₄)₂SO₄) and 100 % organics with no salt (Fig. 7). Liquid–liquid phase separation always tends to lower the critical supersaturation (S_c) and increase the critical diameter (d_c) compared to what is found for the well-mixed case (iv). The lowering of the S_c to $\sim 0.05 \%$ is the least pronounced if liquid–liquid phase separation is preserved but only shell

Table 1. Scenarios for Köhler theory calculations.

Scenario	Phases	Core/shell distr. of water	Shell composition	Surface tension
(i)	LLPS	kinetically hindered	nearly pure organic layer; non-uniform water profile	pure <i>h</i> -CPA ^a
(ii)	LLPS	kinetically hindered	mixed; uniform composition	saturated <i>h</i> -CPA solution ^b
(iii)	LLPS	kinetic hindrance ignored	mixed; uniform composition	saturated <i>h</i> -CPA solution ^b
(iv)	single		mixed; uniform composition	pure water ^c

^a $\gamma = 30 \text{ mN m}^{-1}$ (Hyyvärinen et al., 2006). ^b $\gamma = 60 \text{ mN m}^{-1}$ (Hyyvärinen et al., 2006). ^c $\gamma = 72 \text{ mN m}^{-1}$ (Vargaftik et al., 1983).

growth occurs, which is the scenario (iii) which describes the effect of hindered core uptake without concentration gradient. A moderate lowering of $S_c \sim 0.25\%$ is found for the scenario in which liquid–liquid phase separation maintains moderate surface tension (the surface is a saturated mixture of *h*-CPA and water) with uniform core and shell growth, that is, non-hindered core uptake (ii). Finally, S_c is the lowest if the concentration gradient is taken into account (by assuming a pure organic surface) (i); in this case the critical supersaturation is reduced by $\sim 0.35\%$. Trends are largely similar but more pronounced if the aqueous phase is assumed to contain only organics. In summary, liquid–liquid phase separation – as a result of lower surface tensions characteristic of a saturated mixture – reduces critical supersaturations, while kinetic hindrance of the core uptake acts in the opposite direction since it increases the mole fraction of water in the organic shell. However, the concentration gradient and the resulting low surface tension characteristic of a pure or nearly pure organic surface impart a strong effect and invoke the strongest reduction in S_c compared to the well-mixed case among all the investigated scenarios.

4 Conclusions

Steered MD simulations of water uptake by a model LLPS aerosol particle consisting of a hydroxy-*cis*-pinonic acid surface layer and a pure aqueous core at two temperatures corresponding to the boundary layer (300 K) and to the top of the troposphere (200 K) were performed to investigate the mechanism of water uptake by LLPS aerosol via detailed analysis of the free-energy profiles of the corresponding transfer process. In particular, the following questions were addressed: (i) how does the uptake mechanism depend on temperature? (ii) To what extent and under what conditions can water uptake by particles containing internal interfaces be described with a single uptake coefficient? (iii) What role does the internal interface play in the water uptake mechanism? (iv) How can the relationship between non-ideal mixing in LLPS particles and their increased CCN activity be explained on a molecular level?

These questions are answered using a novel combination of free-energy profiles of interfacial transfer estimated from steered MD simulations and intrinsic surface analysis, which

removes artificial smoothing and systematic errors caused by thermal fluctuations of liquid surfaces from estimates in interfacial properties and density profiles. Free-energy profiles together with their entropic and energetic contributions were used to determine the water uptake mechanism; map the effect of the presence of an internal surface on the shape of the free-energy, energy and entropy profiles; and identify the main thermodynamic driving forces behind the observed mechanism. Using steered MD in this context presents an advancement over previous approaches. The choice of the method can be rationalized by considering that each finite-velocity pulling simulation used for estimating the free energy based on Jarzynski's equality closely mimics one realistic interfacial mass transfer event. The ensemble averaging ensures that a variety of potential pathways is included in the free-energy estimate. Implications for realistic atmospheric processes were presented in the form of model calculations that link the molecular-scale mechanism to the increased CCN activity of LLPS aerosol quantitatively for our model system and qualitatively for generic LLPS particles.

Our findings can be summarized as follows: (i) the mechanism of water uptake (the shape of the free-energy profile) is strongly temperature dependent. All minima and maxima can be attributed to entropic contributions; the minimum at the organic–water interface is due to a local maximum of the conformational entropy, while the subsequent maximum is a consequence of increased ordering of the water molecules in the first molecular layer of the aqueous phase. Due to the explicit temperature dependence of the weight of the entropy term in the free-energy profile, features disappear at low temperature; however structural properties shaping entropy profiles are generally present in liquid–liquid and liquid–solid interfacial systems' arbitrary composition. (ii) Mass accommodation (vapor-to-organic transfer) coefficients were found to be near unity at both temperatures, which is in accordance with globally representative values. The core uptake (organic-to-water transfer) coefficient is reduced at room temperature ($k_{o/w} = 0.03$), while at low temperature $k_{o/w} = 1$. This suggests that a single uptake coefficient is sufficient to describe the water uptake mechanism at 200 K, while core uptake might have to be taken into account for the higher temperature. (iii) Model estimates of shell and core uptake timescales revealed that depending on the particle-phase diffusion coefficient, shell uptake

is at least 4 orders of magnitude faster than that of core transfer. The slow diffusion of water in the organic shell can cause water to accumulate in the shell. This difference is further increased by 1–2 orders of magnitude if the core uptake coefficient is reduced as a result of interfacial ordering of water molecules, leading to even more retention of water in the organic shell. (iv) Converting free-energy profiles into diffusion-corrected concentration profiles allowed us to determine how molecular-scale non-idealities in the solution structure can lead to enhanced surface activity. The molecular-scale explanation of the effect of non-ideal mixing on CCN activity lies in a non-uniform distribution of water molecules within the organic shell observed for liquid particles at 300 K. The concentration distribution has a maximum near the organic–water interface, indicating that the condensing water molecules tend to accumulate near the aqueous phase and leave the surface depleted in water. In other words, the observed concentration gradient maintains low surface tensions (nearly pure organic surface) and the LLPS state even when RH approaches 100 %. Köhler calculations reveal consequent reduced surface tensions are able to compensate for the unfavorable effect on hindered core uptake on critical supersaturations.

In summary, our results point out that a single uptake coefficient is sufficient to describe water uptake in LLPS aerosol at low temperature, while at room temperature the models based on the complete uptake mechanism might be preferred. The effect of non-ideal mixing – usually accounted for in the form of the Flory–Huggins parameter in continuum model calculations – is attributed to non-uniform distributions of the condensing water which maintain surface tension at low values even at high RH. The generalizability of thermodynamic driving forces suggests that the development of detailed models of aerosol growth kinetics incorporating these findings is possible, when combined with more rigorous and quantitative studies.

The strong temperature dependence of the water uptake mechanism and core uptake coefficient, as well as the presence of the non-uniform distribution of water within the organic shell at room temperature, suggests that a detailed description of water uptake including these effects in a temperature-dependent manner is necessary to improve aerosol growth kinetic models. The driving forces responsible for the typical features of the free-energy profiles are generally valid for a wide range of liquid–vapor, liquid–liquid and liquid–solid surfaces. They presumably depend only weakly on the chemical nature of the organic compounds, which suggests that developing such a parametrization is feasible.

Appendix A: Structural analysis

A1 Steered molecular dynamics

In Fig. A1 we demonstrate through the example of three randomly selected realizations from both temperatures that the steered MD trajectories can result in arbitrary impact angles. In the equilibrium snapshots the position of the pulled molecule is shown in the initial configuration and at the point of contact formation with the particle. The organic phase in the snapshots shows the configuration at the moment of impact, but its center of mass has been aligned with that of the initial configurations to ensure that the impact angles are correctly represented.

A2 Intrinsic surface analysis and intrinsic density profiles

We label molecules of the organic–water interface in a time-resolved manner using the ITIM method (Sega et al., 2018). ITIM selects interfacial molecules by solely geometric criteria; thus it is considerably faster than alternative methods with essentially no loss in accuracy (Jorge et al., 2010). The ITIM method uses a probe sphere with a radius determined from the position of the first peak of the corresponding radial distribution functions; in our case a value of $r = 0.2$ nm is used. The probe sphere is moved along a grid of test lines (a 200×200 grid is used in our analysis) perpendicularly to the macroscopic plane of the interface. Once the probe sphere touches an atom, the molecule to which it belongs is labeled as interfacial. Contact is determined based on a Pythagorean criterion. The list of surface molecules allows for selective estimation of various properties of the surface and the bulk and provides a means to reconstruct the intrinsic density profiles:

$$\rho(z) = \frac{1}{A} \left\langle \sum_i \delta_i(z - z_i) + \xi(x_i, y_i) \right\rangle, \quad (\text{A1})$$

where A is the macroscopic surface area of the interface; x_i , y_i and z_i are the Cartesian coordinates of the atoms constituting the system; and z is the position with respect to the local interface. $\xi(x_i, y_i) \sim kT/q^2$ is the capillary wave mode spectrum, with q being the wave vector. In simple terms intrinsic density profiles are anchored to the first molecular layer of one of the condensed phases (the opposite phase in our case), instead of being calculated along an external grid; thus they are able to resolve the near-surface fine structure of the density profiles which are otherwise washed away by capillary wave fluctuations. Intrinsic number density profiles are used to interpret free-energy profiles in a qualitative manner. The ITIM algorithm in particular allows for the separation of the surface molecules from those belonging to the bulk, and thus repeating the algorithm on the remaining bulk-phase molecules can yield consecutive subsurface layers. Separate layers are used to estimate layer-by-layer density profiles as

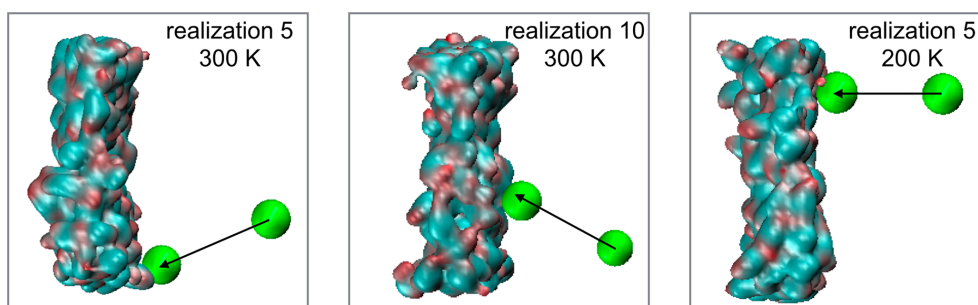


Figure A1. Snapshots showing the impact angle in randomly selected trajectories. The pulled molecule is shown as a green bead while the organic phase is represented by its solvent accessible surface. The aqueous phase was removed from the snapshot for clarity.

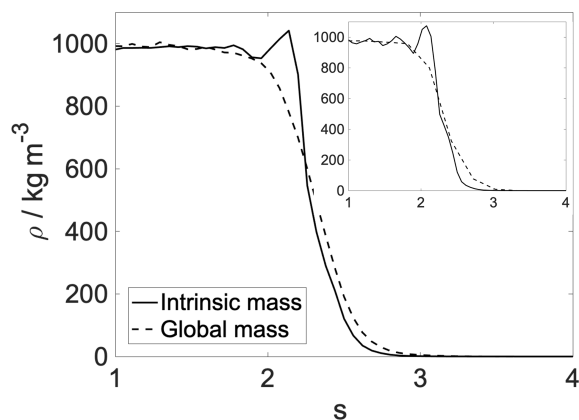


Figure A2. Intrinsic (solid line) and global (dashed line) density profiles of the aqueous phase. Main panel: 300 K; inset: 200 K.

well as orientational distributions within the first two molecular layers of the aqueous phase.

Using intrinsic surface analysis always reveals the layered structure of the near-surface region. Water at room temperature tends to have a very slight layering, with hardly any structure noticeable beyond the second peak (Jorge et al., 2010). Our results show an even less pronounced structure, due to the mixed nature of the interface, which is explained in more detail in the next section. In order to shed light on the enhanced structure that appears only in the intrinsic density profiles, the intrinsic and global mass density profiles of water are overlapped (Fig. A2).

A3 Analysis of the interface structure

In order to clarify the origin of the density drop, which is a non-trivial phenomenon, at least from a macroscopic perspective, we present analysis that highlights the atomistic structure of the organic–water interface. As mentioned before, liquid surfaces are corrugated by capillary waves. These corrugations cause the density drop between the two bulk phases (Jedlovsky et al., 2002; Fernandes et al., 1999; Benjamin, 1997). Depending on the nature of the organic phase

(its solubility in water and the intermolecular interactions that it forms with water molecules), the organic–water interface can be either sharp fully phase separated (e.g., isooctane or heptanone) (Fernandes et al., 1999) or mixed. In the former case the density drop is clearly related to the differing fluctuations of the two sharp surfaces, causing the formation of a thin gap between the two phases. For mixed or interpenetrated interfaces, this effect is somewhat reduced by mixing of the two phases; however voids are still observable as a result of capillary wave fluctuations. Examples of such voids are shown in Fig. A3a. In order to determine whether a liquid–liquid interface is sharp or interpenetrated, one has to examine the sign of the local interface width $W_{ij}(z)$ in elements of a fine perpendicular grid that divides the interface into small elementary units, using the following formula:

$$W_{ij}(z) = \max(L_{ij}(z)) - \min(R_{ij}(z)), \quad (\text{A2})$$

where $L_{ij}(z)$ and $R_{ij}(z)$ are the coordinates of the atoms of the left and right phase, respectively, in the ij th grid cell. A negative sign of the mean width trivially means sharp phase-separated surfaces, while a positive sign means that the interface is mixed. In this work we use a rectangular grid along the surface normal that divides the xy plane into elementary units of the area of 0.04 nm^2 ; the left phase is the aqueous phase, and right phase is the *h*-CPA. Figure A3b shows the histogram of $W_{ij}(z)$ obtained from an equilibrium MD trajectory (3 ns) of the interfacial system, representative of the equilibrium structure of the surface in the absence of a transferred molecule. It is clear that the interface in our system is of the mixed type ($W_{ij}(z)$ assumes almost exclusively positive values). This is consistent with the intrinsic density profile not being exactly zero in the interfacial region. For a fully phase-separated system, the intrinsic density profiles decrease steeply to zero in between the two constituting phases (Jorge et al., 2010).

It is worth noting that the distribution is bimodal, indicating the existence of smaller and larger voids between the two phases. When compared to the mean distance between nearest-neighbor molecules in the bulk phase, estimated as the position of the first intermolecular peak of the corresponding radial distribution function (inset of

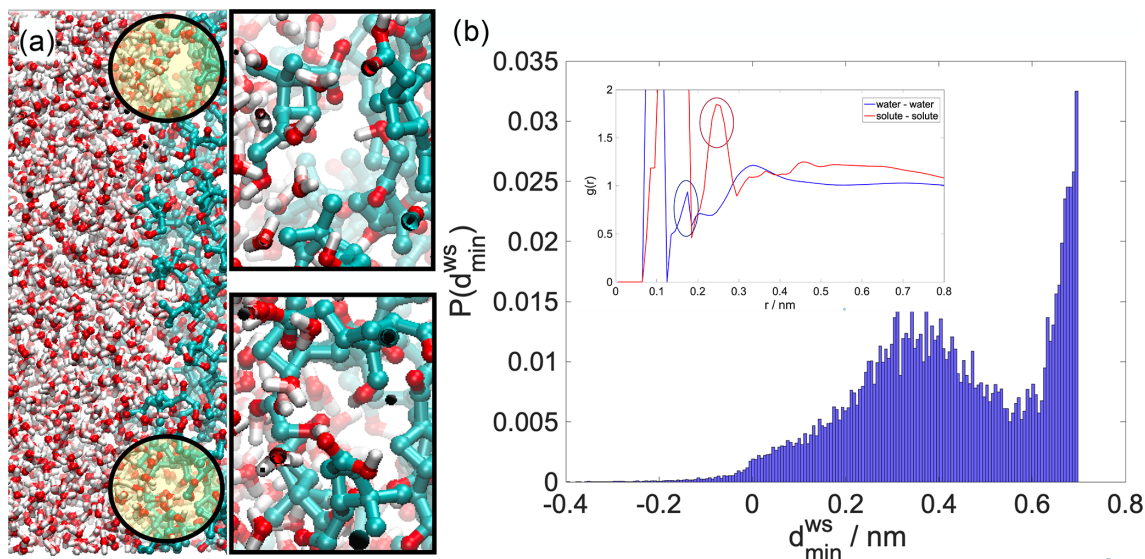


Figure A3. (a) Equilibrium snapshot of the water–organic interface with examples of voids enlarged. The probability distribution of the minimum local distance between the maximum of the aqueous phase and the minimum of the organic phase at the interface in the absence of the pulled molecule. For comparison in the inset we show bulk radial distribution functions whose first intermolecular peaks (circled) can give an estimate of the mean distances in the bulk phases.

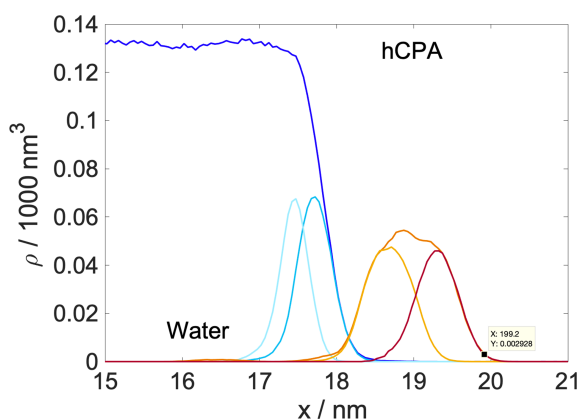


Figure A4. Global number density profiles overlapped with the density profiles of the first two molecular layers detected by the ITIM algorithm. Density profiles are not centered at the center of mass of the aqueous phase.

Fig. A3b), these mean minimal distances are non-negligibly larger. Thus voids in the interface, defined here as the region bounded by the position of the peaks of the intrinsic density profiles, tend to be larger than voids found in any of the bulk phases, which leads to a decrease in the total density. Additionally, as shown in Appendix B, these voids do not reduce the number of hydrogen bonds of the transferring molecule and thus provide a sterically and energetically favorable environment for the pulled water molecule.

A3.1 Interface layering

The density profile of the first two molecular layers detected by the ITIM algorithm are overlapped here with the global intrinsic density profiles.

The width of the first layer of the aqueous phase is 0.48 nm and that of the organic phase 0.7 nm (from the aqueous side) and 0.6 nm (from the vapor side), measured at half of the height of the curves. The large overlap between the first and second molecular layer in the aqueous phase explains the very weak structuring of the subsurface layers. The organic phase is composed of two overlapping interfacial layers, and its width is not sufficient to accommodate any additional layers not in direct contact with any interfaces.

Appendix B: Thermodynamic analysis

The free-energy profiles were decomposed into energetic and various entropic contributions in order to understand the effects responsible for the features observed in the free-energy profiles.

B1 Internal energy and hydrogen bonding

The internal energy profile of the transfer process is estimated as the sum of the interaction energy between the pulled water molecule and the organic and water molecules weighted by the local mole fraction of the solute and the solvent.

$$\Delta E_i(s) = x_s^1(s) \cdot E_i(p, s) + x_w^1(s) \cdot E_i(p, w), \quad (\text{B1})$$

with $E_i(p, s)$ and $E_i(p, w)$ being the interaction energy between the pulled molecule and the solutes/water, calculated as the sum of short-term coulombic and Lennard-Jones interactions (example values are listed in Table B1). $x_s^l(s)$ and $x_w^l(s)$ are local mole fraction profiles of the water and the organics. Local mole fraction profiles are calculated from the number of water and organic molecules found within 1 nm of the pulled molecule. The cutoff distance of 1 nm corresponds to the cutoff used in the simulations for short-range interactions. This calculation is only plausible because solute–water interactions in the OPLS and TIP4P force fields were parametrized partially on quantum chemical calculations; thus individual interaction energies are physically meaningful. Equation (B1) is evaluated for all realizations and averaged to yield the final profiles. Internal energy profiles of selected realizations are shown in Fig. B1.

The formation of hydrogen bonds is a major energetic driving force of the water uptake process. Figure B2 shows the number of total hydrogen bonds along the direction of the reaction coordinate.

B2 Entropy

B2.1 Interfacial entropy

Interfacial entropy accompanying any molecular transfer across phase boundaries can be calculated using the following formula from statistical thermodynamics (Ward, 2002):

$$\begin{aligned} \frac{\Delta S_{\text{IF}}}{k} = & 4 \left(1 - \frac{T_L}{T_V} \right) + \left(\frac{1}{T_L} - \frac{1}{T_V} \right) \\ & \sum_{l=1}^3 \left(\frac{\hbar \omega_l}{2k} + \frac{\hbar \omega_l / k}{\exp(\hbar \omega_l / k T_V) - 1} \right) \\ & + \frac{v_L^{\text{sat}}}{k T_L} \left[P_V - P_{\text{sat}}(T_L) \right] \\ & + \ln \left[\left(\frac{T_L}{T_V} \right)^4 \left[\frac{P_{\text{sat}}(T_L)}{P_V} \right] \right] \\ & + \ln \left[\frac{q_{\text{vib}}(T_V)}{q_{\text{vib}}(T_L)} \right], \end{aligned} \quad (\text{B2})$$

where T_V and T_L are the temperatures of the vapor and the liquid phase, P_{sat} and P_V are the saturated and the actual vapor pressure, v_L is the specific volume of the liquid phase, ω_i comprises the vibrational frequencies, and q_{vib} is the vibrational partition function. Figure B3 shows the modeled $T \Delta S_{\text{IF}}$ profiles at the two simulated temperatures; the values corresponding to the vapor pressures in the simulation box are highlighted with asterisks. The vapor pressure in the simulation box is estimated assuming the presence of the pulled molecule only in the vapor phase, using the universal gas law.

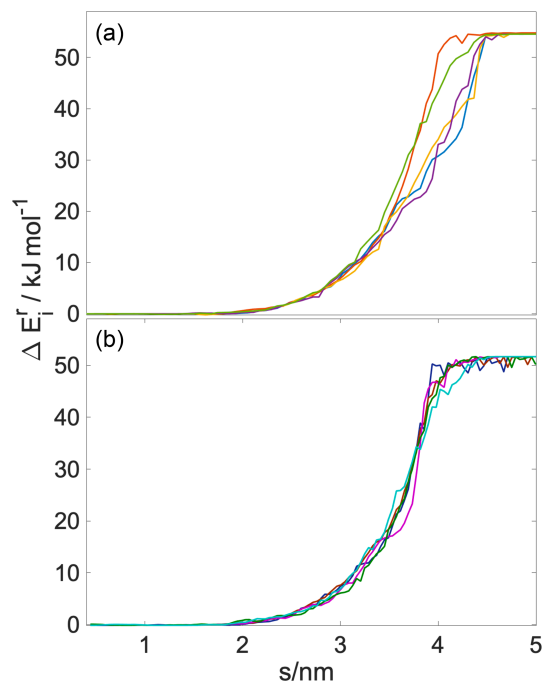


Figure B1. Internal energy profiles of selected realizations: (a) 200 and (b) 300 K.

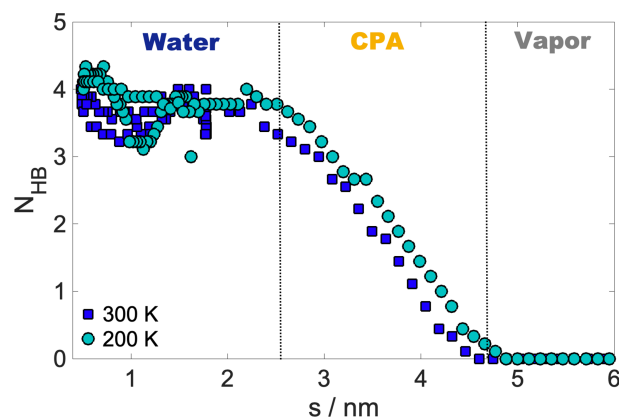
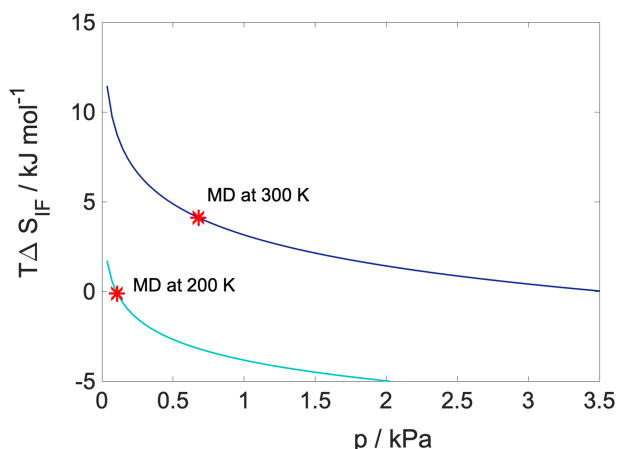


Figure B2. The number of hydrogen bonds formed by the pulled molecules along the reaction coordinate.

Table B1. Coulombic and Lennard-Jones (LJ) contributions of the interaction energies in selected realizations.

Type	R1		R2		R3	
	200 K	300 K	200 K	300 K	200 K	300 K
LJ(p, s)	0.2 (0.1)	−0.3 (0.07)	−0.43 (0.2)	−0.2 (0.02)	−0.09 (0.02)	−0.09 (0.06)
Coulomb(p, s)	−5.7 (1.3)	−3.4 (1.1)	−5.4 (2.1)	−3.7 (1.2)	−6.8 (3)	−3.8 (1.3)
LJ(p, w)	14.4 (1.9)	11.3 (1.5)	15.1 (2.2)	11.1 (1.4)	14.2 (2.1)	10.9 (1.4)
Coulomb(p, w)	−74.5 (10.5)	−66.5 (8.5)	−75.7 (10.4)	−66.4 (8.2)	−71.8 (10.2)	−65.6 (1.0)

**Figure B3.** Modeled interfacial entropies at the simulated temperatures.

B2.2 Conformational entropy

The conformational entropy profile is estimated as

$$S_{\text{conf}} = -k_B \sum_i x_i(s) \ln(x_i(s)), \quad (\text{B3})$$

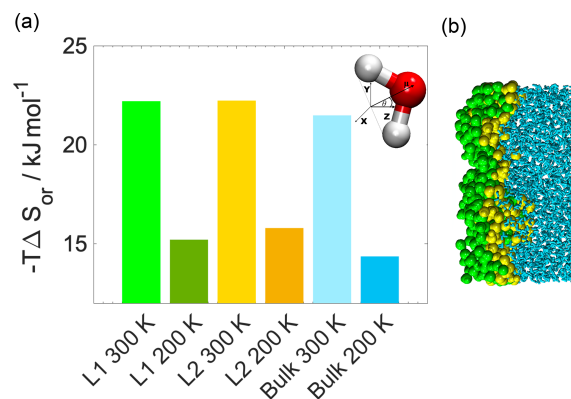
where $x_i(s)$ denotes mole fraction profiles of the components of the systems, with s being the reaction coordinate used in the steered MD simulations.

B2.3 Configurational entropy

We calculate configurational entropy according to Schlitter's formula (Baron et al., 2006), thus based on the covariance matrix (**D**) of the atomic coordinates between two distinct groups of atoms, one being the pulled molecule and the other the ensemble of either the solutes or the waters constituting the bulk phase.

$$S_{\text{config}} = \frac{k_B}{2} \ln \left(1 + \frac{k_B T e^2}{h} \mathbf{D} \right), \quad (\text{B4})$$

where h is Planck's constant divided by 2π . Two different contributions of the configurational entropy are considered (i) between the pulled molecule and the solutes and (ii) between the pulled molecule and the solvents. In a similar manner to for the internal energy, the weighted sum of these two

**Figure B4.** (a) Orientational entropies in the first and second molecular layers and the bulk phase for both simulated temperatures. Inset: the definition of the θ angle. (b) Snapshot from a 300 K realization showing the first two molecular layers of the aqueous phase in green (L1) and yellow (L2).

contributions yields the configurational entropy profile along the reaction coordinate (s), with the weights being the local mole fractions of the water and the solute, whose calculation is described in the previous section.

B2.4 Orientational entropy

We propose an equation which can serve as a qualitative descriptor of the entropy related to the orientation of the molecules based on equations for translational (Bhandary et al., 2016) and translational-orientation entropy terms (Piggi and Parrinello, 2018). With a simple exchange of the radial distribution function in Bhandary et al. (2016) with the angular distribution function ($g(\theta)$) of the angle (θ) between the dipole vector of the water molecules and the surface-normal axis, we obtain an expression for orientational entropy:

$$S_{\text{or}} = -2\pi k_B \int [g(\theta) \ln g(\theta) - g(\theta) + 1] \sin \theta d\theta. \quad (\text{B5})$$

This expression is evaluated for angular distribution functions calculated in the first two molecular layers and the bulk of the aqueous phase, to highlight the effect of increased molecular order on the free-energy profiles. The separation of interfacial water molecules and those constituting the sec-

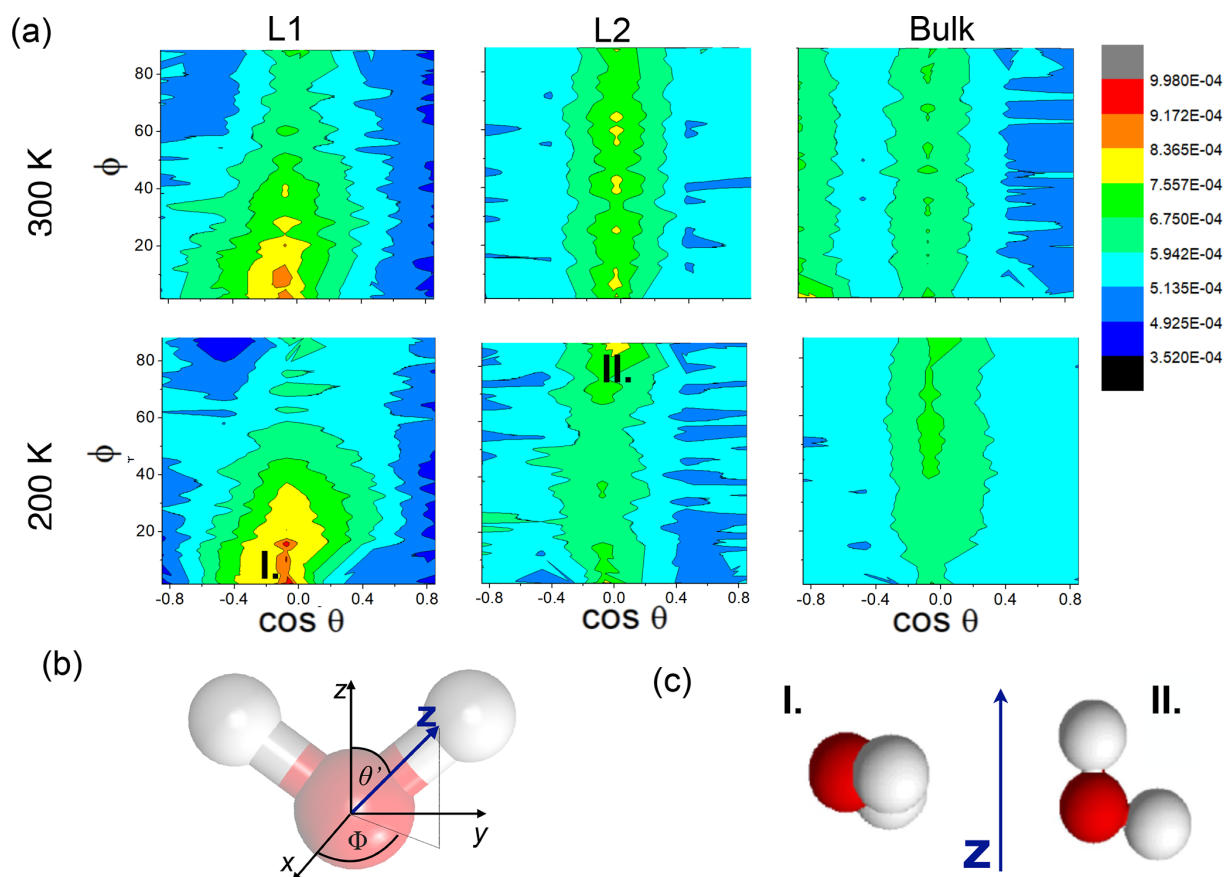


Figure B5. (a) Orientational maps of the water molecules in the first (L1) and second (L2) molecular layer and the bulk phase. (b) The definition of θ' and ϕ in the Cartesian frame centered on a water molecule. (c) Examples of the two main orientations.

ond layer is performed by two consecutive repetitions of the ITIM algorithm, using the output bulk phase of the first one as input for the second one.

At both temperatures the bulk-phase orientational entropy is higher ($-T\Delta S$ is lower) than in the first two layers due to stronger ordering in the first two interfacial layers (Fig. B4). We note that Eq. (B5) cannot completely describe the entropy loss due to preferential ordering of the water molecules at the interface since due to its point group symmetry (C_{2v}), the orientation of water molecules with respect to an external vector or plane cannot be described with a single angle; instead the joint distribution of two angles is necessary. The development of an adapted expression of the orientational entropy of such cases is however out of the scope of this study. The one-dimensional representation is incomplete and thus gives only a qualitative insight, but the temperature dependence of $T\Delta S_{\text{or}}$ within the layers is clear; the extension of the orientational entropy formula to multiple dimensions is part of ongoing work. To complete the description of orientational differences between the surface and the bulk of the aqueous phase, we calculate joint distributions of angles $\cos \theta'$ and ϕ , which are chosen to fully describe the orientation of water molecules with respect to the normal vector of the macro-

scopic surface (Bartók-Pártay et al., 2008), in the first two molecular layers and the bulk. θ' and ϕ are defined in a Cartesian frame centered on the water molecules; the z axis points from the water oxygen towards the midpoint of the segment connecting the hydrogen atoms; the y axis is parallel to that segment, and the x axis is perpendicular to both z and y . θ' is the angle between the macroscopic surface-normal vector (z) and the molecule-centered z axis, and ϕ is the angle between the x axis and the projection of the surface-normal vector to the x,y plane.

Figure B5 shows orientational maps in the first two molecular layers and the bulk of the aqueous phase. In the first layer water molecules show a very strong preference to be aligned with dipole vectors parallel to the surface or slightly tilted towards the bulk aqueous phase, orientation I in Fig. B5a and c. In another distinguished orientation, which appears in the first and second layer at 300 K and the second layer at 200 K, one O–H bond points in the direction of the surface-normal vector and the other slightly inwards to the bulk aqueous phase. Orientational preferences diminish progressively when moving towards the bulk phase, indicating the decrease in orientational order and thus an increase in orientational entropy. It is a remarkable difference between our

system and aqueous interfaces of hydrophobic organic compounds (dichloromethane and dichloroethane) studied previously (Hantal et al., 2010), where preferred orientations were only found in the first molecular layer of water in direct contact with the organic phase, that the second layer is more ordered than the bulk phase; this is due to the fact that *h*-CPA mixes more readily with water than hydrophobic organics. Thus *h*-CPA molecules can penetrate into the second and third molecular layer as well into the bulk phase, and contact with the dissolved organic molecules promotes orientations that are similar to those found at the interface. We also note that the preferred orientations found of interfacial waters are universal across a large spectra of organic–water interfaces.

Appendix C: Statistical analysis

C1 Statistical accuracy of the results

The statistical accuracy of the free-energy profiles is assessed using an approach inspired by bootstrapping, which has already been used to analyze the statistical accuracy as a function of sample size for steered MD simulations (Potterton et al., 2019). Free-energy profiles are calculated on subsets of the whole sample size containing a varying number of realizations, created by removing $n = [1, 22]$ randomly selected trajectories from the total number of samples. A total of 10 different random samples of each size are generated and then used to estimate mean free-energy profiles, their standard deviation and 95 % confidence intervals at each sample size.

Figure C1a shows the free-energy profiles at 300 and 200 K estimated from different numbers of samples. At 300 K the free-energy profiles become nearly invariant with the number of samples for sample sizes superior to 75, above which also the standard deviation of the free energy in each point of the profile becomes considerably smaller than for smaller samples. A smaller number of samples suffice to produce converged free-energy profiles at 200 K.

Figure C2 shows the value of the free energy in the vapor phase and at the free-energy maximum at 200 and 300 K as a function of sample size, with their 95 % confidence intervals and their standard deviation to assess statistical accuracy by comparing them against $k_B T$ at the given temperature. In classical molecular simulations the energy of the thermal motion ($3/2k_B T$) is often considered the limit of statistical significance. Here we compare to a stricter criterion; i.e., we compare the changes in the mean values with the sample size, their standard deviation and their 95 % confidence interval to the value of the Boltzmann factor and accept the free energy as statistically accurate if the changes in the mean value upon increasing the sample size are smaller than $k_B T$ and both the standard deviation and the confidence interval fall within a range of $\pm 1/2k_B T$ from the mean value of the free-energy (ΔG). According to this assessment at 300 K the number of samples necessary to reproduce statistically sig-

nificant vapor-phase free-energy values is 75; for the maxima 65 samples are sufficient. At 200 K these criteria are fulfilled already at the smallest sample size containing 60 realizations. From this analysis we conclude that our free-energy profiles estimated from 82 realizations can be considered converged and statistically significant within a range of uncertainty that can be attributed to thermal motion at the temperature of interest.

C2 Thermodynamic consistency of the data

C2.1 Vapor-phase internal energy and enthalpy of evaporation

The heat of vaporization, calculated as the difference in the internal energy of the vapor and the aqueous phase is $\sim 55 \text{ kJ mol}^{-1}$ at 300 K and $\sim 60 \text{ kJ mol}^{-1}$ at 200 K, the latter extrapolated from the lowest available temperatures (240–250 K) assuming a linear fit (from the Dortmund Data Bank, 2021, <http://www.ddbst.com>, last access: 10 September 2021). The latent heat values of the vaporization of pure water, 43.9 kJ mol^{-1} at 300 K and 58 kJ mol^{-1} at 200 K, are within 25 % and 4 % of the simulated values. This is not a direct comparison, since the presence of the organic layer potentially impacts the latent heat of vaporization to an unknown extent; however the trend is well reproduced and the percentile differences indicate a semi-quantitative agreement with the experimental values.

C2.2 Comparison with experimentally derived free energies of transfer

The difference between the vapor and liquid phase end of the simulated free-energy profiles corresponds to the free-energy change related to the transfer of a single water molecule from the liquid phase to the vapor phase ($\Delta_v^l G$, the free-energy change that accompanies the evaporation of a single molecule). The free energy of transfer between two phases of different density can be estimated from the density of the transferred molecule in the liquid (ρ_l^t) and the vapor phase (ρ_v^t) (Ben-Naim, 1978; Wick et al., 2003; Martin and Siepmann, 1998). For evaporation the equation takes the form of

$$\Delta_v^l G = -RT \ln \frac{\rho_v^t}{\rho_l^t}. \quad (\text{C1})$$

In our model calculation ρ_l^t is the density of the pure water at the temperature of interest. To the best of our knowledge, at 200 K measurements of experimental densities of either supercooled water or ice are not available; therefore the values of the lowest measured temperatures are used in the calculation. ρ_v^t is simply estimated from the universal gas law as p/RT , assuming that water vapor behaves as ideal gas under atmospherically relevant conditions. The vapor pressure of supercooled water and ice is estimated from parametric equations (Wexler et al., 1977; Mauersberger and Krankowsky,

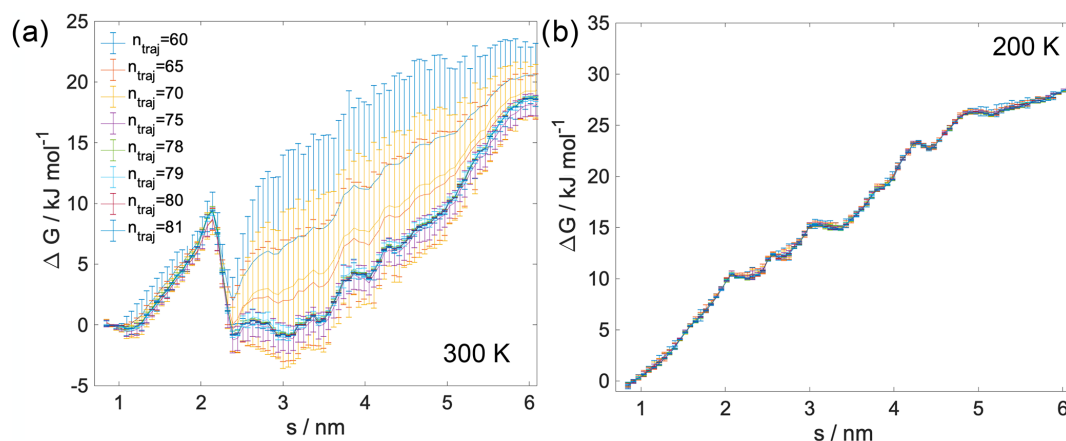


Figure C1. Mean free-energy profiles with varying sample sizes at (a) 300 and (b) 200 K. Error bars represent 1 standard deviation.

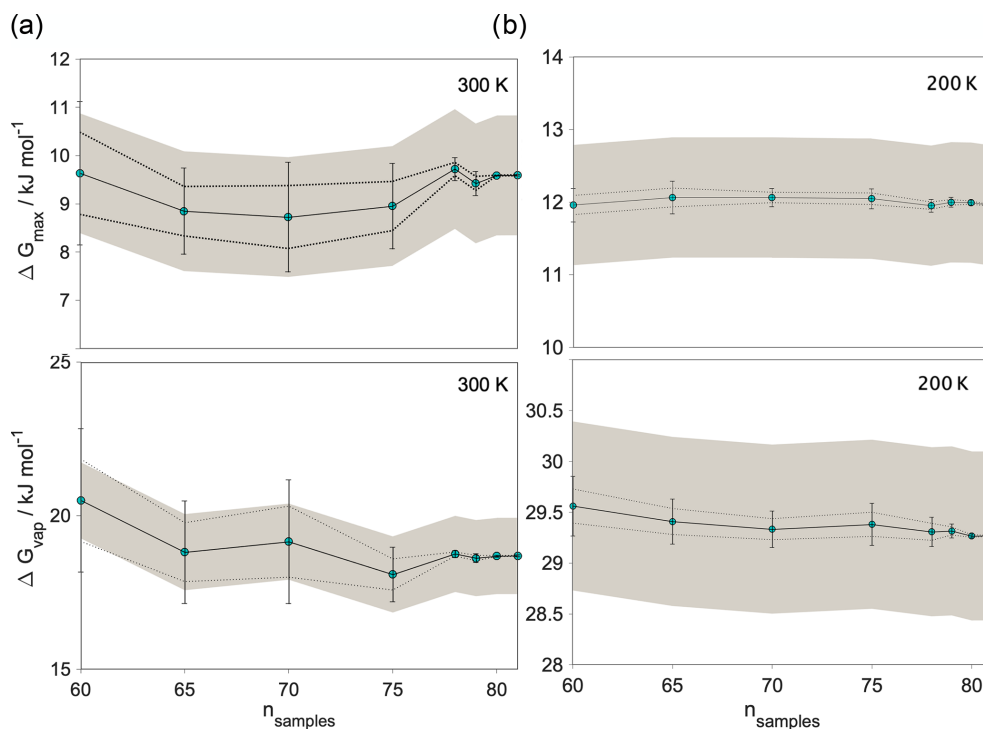


Figure C2. (a) Top panel: value of the free energy in the vapor phase at 300 K. Bottom panel: the maximum of the free energy in the bulk liquid phase at 300 K. (b) Top panel: value of the free energy in the vapor phase at 200 K. Bottom panel: the maximum of the free energy in the bulk liquid phase at 200 K. The error bars represent 1 standard deviation; dotted lines are the 95 % confidence intervals, and the grey-shaded area indicates the region that falls within $\pm 1/2k_B T$ of the mean values.

2003; Murphy and Koop, 2005). Table C1 summarizes the data used in the calculations and the free-energy differences obtained.

From our simulations $\Delta_v^l G$ is 19.7 kJ mol^{-1} at 300 K and 29.4 kJ mol^{-1} at 200 K. Our simulations systematically underestimate the free-energy differences predicted from Eq. (C1) by 7 and by 2 kJ mol^{-1} at the two temperatures, 300 and 200 K, respectively. However, given that the statistical errors are much smaller than the difference between $\Delta_v^l G$

at the simulated temperatures, we can conclude that the temperature dependence is well reproduced.

Gibbs ensemble Monte Carlo simulations yield 23 kJ mol^{-1} at 300 K and 25 kJ mol^{-1} at 273 K for pure TIP5P water (Wick et al., 2003). They lead to the conclusion that the underestimation of the free energy of transfer at a given temperature and the overestimation of the temperature dependence are caused by the fact that the TIP5P water model, optimized to reproduce specific density

Table C1. Estimates of the free energy of transfer based on experimental data.

Condensed phase	T (K)	p_v (Pa)	ρ_v^l (m ⁻³)	ρ_l^l (m ⁻³)	$\Delta_v^l G$ (kJ mol ⁻¹)
Liquid water	300	353	0.85×10^{23}	33.23×10^{27}	26.35
Supercooled water	200	0.5 ^a	18.04×10^{19}	32.60×10^{27b}	31.56
Ice	200	0.26 ^c	9.38×10^{19}	30.76×10^{27d}	32.54
Ice	200	0.46 ^e	16.59×10^{19}	30.76×10^{27}	31.60

^a Vapor pressure over supercooled water taken from the parametrization of Murphy and Koop (2005). ^b Density of supercooled water at 239 K (Liu et al., 2008). ^c Vapor pressure over ice taken from the parametrization of Wexler et al. (1977). ^d Density of ice at 223 K (Raznjevic, 1976). ^e Vapor pressure over ice taken from the parametrization of Mauersberger and Krankowsky (2003).

at the density maximum and the liquid structure at room temperature, cannot reproduce the free energy of transfer in a quantitative manner (Wick et al., 2003). Umbrella-sampling simulations (Ergin and Takahama, 2016) yield a value of $\Delta_v^l G = 24 \text{ kJ mol}^{-1}$ for the SPC/E water model, which is known to underestimate the vapor pressure at room temperature (Vega et al., 2006). The TIP4P water model is among the best to reproduce hydrogen bonding in the condensed phase (Zielkiewicz, 2005), as well as the vapor pressure of water as a function of temperature (Vega et al., 2006). However, it still overestimates the experimental vapor pressure by a factor of ~ 1.2 , which may slightly contribute to the underestimation of the free-energy differences. More likely the observed difference is due to the presence of the organic coating and the fact that the aqueous phase of our system at 300 K is not pure water but an aqueous solution of *h*-CPA, which can contribute to the difference between experimental and simulated values. Since we use a very simple transferable potential to represent the organic compound, we cannot expect our simulations to provide a quantitative estimate of the free energy of transfer.

In conclusion, we cannot reach quantitative agreement between our simulations and the free-energy differences estimated from the vapor pressure and the liquid-phase density. This is partially due to limitations of the force field and partially to the fact that no direct comparison can be made between the aqueous phase in our simulation at room temperature and pure water. However, trends are well reproduced and a semi-quantitative agreement with experiments is achieved, which is sufficient to support our conclusions.

Data availability. PLUMED input files and starting configurations are available upon request. A movie showing a sample steered MD trajectory at 300 K is available at https://zenodo.org/record/4902870#.YLSZwS0Rq_U (Lbadaoui-Darvas et al., 2021).

Author contributions. MLD designed and performed simulations and analysis and wrote the manuscript. ST and AN contributed to analysis, interpreted results, and wrote the manuscript.

Competing interests. The contact author has declared that neither they nor their co-authors have any competing interests.

Disclaimer. Publisher's note: Copernicus Publications remains neutral with regard to jurisdictional claims in published maps and institutional affiliations.

Financial support. This research has been supported by the Swiss National Science Foundation (grant nos. CRSK-2_195329 and 200021_169506) and the European Research Council, Horizon 2020 (PyroTRACH, project ID 726165, and FORCEs, grant no. 821205).

Review statement. This paper was edited by Barbara Ervens and reviewed by two anonymous referees.

References

- Abraham, M. J., Murtola, T., Schulz, R., Páll, S., Smith, J. C., Hess, B., and Lindahl, E.: GROMACS: High Performance Molecular Simulations through Multi-level Parallelism from Laptops to Supercomputers, *SoftwareX*, 1/2, 19–25, <https://doi.org/10.1016/j.softx.2015.06.001>, 2015.
- Allen, W. J., Wiley, M. R., Myles, K. M., Adelman, Z. N., and Bevan, D. R.: Steered molecular dynamics identifies critical residues of the Nodamura virus B2 suppressor of RNAi, *J. Molecul. Model.*, 20, 2092, <https://doi.org/10.1007/s00894-014-2092-0>, 2014.
- Bahadur, R. and Russell, L.: Water uptake coefficients and deliquescence of NaCl nanoparticles at atmospheric relative humidities from molecular dynamics simulations, *J. Chem. Phys.*, 129, 094508, <https://doi.org/10.1063/1.2971040>, 2008.
- Barclay, P. L. and Lukes, J. R.: Curvature dependence of the mass accommodation coefficient, *Langmuir*, 35, 6196–6202, 2019.
- Baron, R., de Vries, A. H., Hünenberger, P. H., and van Gunsteren, W. F.: Configurational Entropies of Lipids in Pure and Mixed Bilayers from Atomic-Level and Coarse-Grained Molecular Dynamics Simulations, *J. Phys. Chem. B*, 110, 15602–15614, <https://doi.org/10.1021/jp061627s>, 2006.

- Bartók-Pártay, L., Horvai, G., and Jedlovsky, P.: Molecular level structure of the liquid/liquid interface. Molecular dynamics simulation and ITIM analysis of the water-CCl₄ system, *Phys. Chem. Chem. Phys.*, 10, 4754–64, <https://doi.org/10.1039/b807299j>, 2008.
- Ben-Naim, A.: Standard thermodynamics of transfer. Uses and misuses, *J. Phys. Chem.*, 82, 792–803, 1978.
- Benjamin, I.: Molecular structure and dynamics at liquid-liquid interfaces, *Annu. Rev. Phys. Chem.*, 48, 407–451, <https://doi.org/10.1146/annurev.physchem.48.1.407>, 1997.
- Benjamin, I.: Hydronium ion at the water/1, 2-dichloroethane interface: Structure, thermodynamics, and dynamics of ion transfer, *J. Chem. Phys.*, 151, 094701, <https://doi.org/10.1063/1.5116008>, 2019.
- Benjamin, I.: Mechanism and dynamics of ion transfer across a liquid-liquid interface, *Science*, 261, 1558–1560, 1993.
- Bhandary, D., Benková, Z., Cordeiro, M. N. D. S., and Singh, J. K.: Molecular dynamics study of wetting behavior of grafted thermo-responsive PNIPAAm brushes, *Soft Matter*, 12, 3093–3102, <https://doi.org/10.1039/C5SM02684A>, 2016.
- Braga, C., Muscatello, J., Lau, G., Müller, E. A., and Jackson, G.: Nonequilibrium study of the intrinsic free-energy profile across a liquid-vapour interface, *J. Chem. Phys.*, 144, 044703, <https://doi.org/10.1063/1.4940137>, 2016.
- Bresme, F., Chacón, E., and Tarazona, P.: Molecular dynamics investigation of the intrinsic structure of water–fluid interfaces via the intrinsic sampling method, *Phys. Chem. Chem. Phys.*, 10, 4704–4715, <https://doi.org/10.1039/B807437M>, 2008.
- Bussi, G., Donadio, D., and Parrinello, M.: Canonical Sampling through Velocity Rescaling, *J. Chem. Phys.*, 126, 014101, <https://doi.org/10.1063/1.2408420>, 2007.
- Bzdek, B. R. and Reid, J. P.: Perspective: Aerosol microphysics: From molecules to the chemical physics of aerosols, *J. Chem. Phys.*, 147, 220901, <https://doi.org/10.1063/1.5002641>, 2017.
- Cipcigan, F., Sokhan, V., Jones, A., Crain, J., and Martyna, G.: Hydrogen bonding and molecular orientation at the liquid–vapour interface of water, *Phys. Chem. Chem. Phys.*, 17, 8660–8669, <https://doi.org/10.1039/C4CP05506C>, 2015.
- Clement, C. F., Kulmala, M., and Vesala, T.: Theoretical consideration on sticking probabilities, *J. Aerosol Sci.*, 27, 869–882, [https://doi.org/10.1016/0021-8502\(96\)00032-8](https://doi.org/10.1016/0021-8502(96)00032-8), 1996.
- Cuendet, M. A.: The Jarzynski identity derived from general Hamiltonian or non-Hamiltonian dynamics reproducing NVT or NPT ensembles, *J. Chem. Phys.*, 125, 144109, <https://doi.org/10.1063/1.2338535>, 2006.
- Darvas, M., Pojják, K., Horvai, G., and Jedlovsky, P.: Molecular dynamics simulation and identification of the truly interfacial molecules (ITIM) analysis of the liquid-vapor interface of dimethyl sulfoxide, *J. Chem. Phys.*, 132, 134701, <https://doi.org/10.1063/1.3368111>, 2010a.
- Darvas, M., Pártay, L. B., Jedlovsky, P., and Horvai, G.: Computer simulation and ITIM analysis of the surface of water–methanol mixtures containing traces of water, *J. Mol. Liq.*, 153, 88–93, <https://doi.org/10.1016/j.molliq.2009.06.004>, 2010b.
- Darvas, M., Gilányi, T., and Jedlovsky, P.: Competitive Adsorption of Surfactants and Polymers at the Free Water Surface, A Computer Simulation Study of the Sodium Dodecyl Sulfate–Poly(ethylene oxide) System, *J. Phys. Chem. B*, 115, 933–944, <https://doi.org/10.1021/jp110270c>, PMID: 21250730, 2011a.
- Darvas, M., Jorge, M., D. S. Cordeiro, M. N., and Jedlovsky, P.: Solvation Free Energy Profile of the SCN[−] Ion across the Water–1,2-Dichloroethane Liquid/Liquid Interface, A Computer Simulation Study, *J. Phys. Chem. C*, 115, 11140–11146, <https://doi.org/10.1021/jp2018605>, 2011b.
- Darvas, M., Hoang, P. N., Picaud, S., Sega, M., and Jedlovsky, P.: Anesthetic molecules embedded in a lipid membrane: a computer simulation study, *Phys. Chem. Chem. Phys.*, 14, 12956–12969, 2012.
- Darvas, M., Jorge, M., Cordeiro, M. N. D. S., Kantorovich, S. S., Sega, M., and Jedlovsky, P.: Calculation of the Intrinsic Solvation Free Energy Profile of an Ionic Penetrant Across a Liquid–Liquid Interface with Computer Simulations, *J. Phys. Chem. B*, 117, 16148–16156, <https://doi.org/10.1021/jp404699t>, 2013.
- Davidovits, P., Worsnop, D., Jayne, J., Kolb, C., Winkler, P., Vrtala, A., Wagner, P., Kulmala, M., Lehtinen, K., Vesala, T., and Mozurkewich, M.: Mass accommodation coefficient of water vapor on liquid water, *Geophys. Res. Lett.*, 31, L22111, <https://doi.org/10.1029/2004GL020835>, 2004.
- Davies, J., Miles, R., Haddrell, A., and Reid, J.: Influence of organic films on the evaporation and condensation of water in aerosol, *P. Natl. Acad. Sci. USA*, 110, 8807–8812, <https://doi.org/10.1073/pnas.1305277110>, 2013.
- Diveky, M. E., Roy, S., Cremer, J. W., David, G., and Signorell, R.: Assessing relative humidity dependent photoacoustics to retrieve mass accommodation coefficients of single optically trapped aerosol particles, *Phys. Chem. Chem. Phys.*, 21, 4721–4731, <https://doi.org/10.1039/C8CP06980H>, 2019.
- Einstein, A.: Über einen die Erzeugung und Verwandlung des Lichtes betreffenden heuristischen Gesichtspunkt, *Ann. Phys.*, 322, 132–148, 1905.
- Ergin, G. and Takahama, S.: Carbon Density Is an Indicator of Mass Accommodation Coefficient of Water on Organic-Coated Water Surface, *J. Phys. Chem. A*, 120, 2885–2893, <https://doi.org/10.1021/acs.jpca.6b01748>, PMID: 27089481, 2016.
- Essmann, U., Perera, L., Berkowitz, M. L., Darden, T., Lee, H., and Pedersen, L. G.: A Smooth Particle Mesh Ewald Method, *J. Chem. Phys.*, 103, 8577–8593, 1995.
- Facchini, M. C., Mircea, M., Fuzzi, S., and Charlson, R. J.: Cloud albedo enhancement by surface-active organic solutes in growing droplets, *Nature*, 401, 257–259, <https://doi.org/10.1038/45758>, 1999.
- Fernandes, P. A., Cordeiro, M. N. D. S., and Gomes, J. A. N. F.: Molecular Dynamics Study of the Transfer of Iodide across Two Liquid/Liquid Interfaces, *J. Phys. Chem. B*, 103, 8930–8939, <https://doi.org/10.1021/jp9916945>, 1999.
- Fuzzi, S., Andreae, M. O., Huebert, B. J., Kulmala, M., Bond, T. C., Boy, M., Doherty, S. J., Guenther, A., Kanakidou, M., Kawamura, K., Kerminen, V.-M., Lohmann, U., Russell, L. M., and Pöschl, U.: Critical assessment of the current state of scientific knowledge, terminology, and research needs concerning the role of organic aerosols in the atmosphere, climate, and global change, *Atmos. Chem. Phys.*, 6, 2017–2038, <https://doi.org/10.5194/acp-6-2017-2006>, 2006.
- Ghatee, M. H., Zolghadr, A. R., Moosavi, F., and Pakdel, L.: The extent of molecular orientation at liquid/vapor interface of pyri-

- dine and its alkyl derivatives by molecular dynamics simulation, *J. Chem. Phys.*, 134, 074707, <https://doi.org/10.1063/1.3554361>, 2011.
- Gore, J., Ritort, F., and Bustamante, C.: Bias and error in estimates of equilibrium free-energy differences from nonequilibrium measurements, *P. Natl. Acad. Sci. USA*, 100, 12564–12569, <https://doi.org/10.1073/pnas.1635159100>, 2003.
- Gorkowski, K., Donahue, N. M., and Sullivan, R. C.: Emulsified and liquid–liquid phase-separated states of α -pinene secondary organic aerosol determined using aerosol optical tweezers, *Environ. Sci. Technol.*, 51, 12154–12163, 2017.
- Gorkowski, K., Donahue, N. M., and Sullivan, R. C.: Aerosol Optical Tweezers Constrain the Morphology Evolution of Liquid–Liquid Phase-Separated Atmospheric Particles, *Chem*, 6, 204–220, <https://doi.org/10.1016/j.chempr.2019.10.018>, 2020.
- Grote, R. F. and Hynes, J. T.: The stable states picture of chemical reactions. II. Rate constants for condensed and gas phase reaction models, *J. Chem. Phys.*, 73, 2715–2732, 1980.
- Hantal, G., Darvas, M., Pártay, L. B., Horvai, G., and Jedlovsky, P.: Molecular level properties of the free water surface and different organic liquid/water interfaces, as seen from ITIM analysis of computer simulation results, *J. Phys. Cond. Matt.*, 22, 284112, <https://doi.org/10.1088/0953-8984/22/28/284112>, 2010.
- Hummer, G. and Szabo, A.: Free energy reconstruction from nonequilibrium single-molecule pulling experiments, *P. Natl. Acad. Sci. USA*, 98, 3658–3661, <https://doi.org/10.1073/pnas.071034098>, 2001.
- Hyvärinen, A.-P., Lihavainen, H., Gaman, A., Vairila, L., Ojala, H., Kulmala, M., and Viisanen, Y.: Surface Tensions and Densities of Oxalic, Malonic, Succinic, Maleic, Malic, and cis-Pinonic Acids, *J. Chem. Eng. Data*, 51, 255–260, <https://doi.org/10.1021/je050366x>, 2006.
- IPCC: Summary for Policymakers, in: *Climate Change 2021: The Physical Science Basis*, Contribution of Working Group I to the Sixth Assessment Report of the Intergovernmental Panel on Climate Change, edited by: Masson-Delmotte, V., Zhai, P., Pirani, A., Connors, S. L., Péan, C., Berger, S., Caud, N., Chen, Y., Goldfarb, L., Gomis, M. I., Huang, M., Leitzell, K., Lonnoy, E., Matthews, J. B. R., Maycock, T. K., Waterfield, T., Yelekçi, O., Yu, R., and Zhou, B., Cambridge University Press, in press, 2021.
- Jarzynski, C.: Nonequilibrium Equality for Free Energy Differences, *Phys. Rev. Lett.*, 78, 2690–2693, <https://doi.org/10.1103/PhysRevLett.78.2690>, 1997.
- Jedlovsky, P., Vincze, A., and Horvai, G.: New Insight into the Orientational Order of Water Molecules at the Water/1,2-Dichloroethane Interface: A Monte Carlo Simulation Study, *J. Chem. Phys.*, 117, 2271–2280, <https://doi.org/10.1063/1.1488579>, 2002.
- Johansson, S. M., Lovrić, J., Kong, X., Thomson, E. S., Hallquist, M., and Pettersson, J. B. C.: Experimental and Computational Study of Molecular Water Interactions with Condensed Nopinone Surfaces Under Atmospherically Relevant Conditions, *J. Phys. Chem. A*, 124, 3652–3661, <https://doi.org/10.1021/acs.jpca.9b10970>, 2020.
- Jorge, M., Hantal, G., Jedlovsky, P., and Cordeiro, M. N. D. S.: A Critical Assessment of Methods for the Intrinsic Analysis of Liquid Interfaces: 2. Density Profiles, *J. Phys. Chem. C*, 114, 18656–18663, <https://doi.org/10.1021/jp107378s>, 2010.
- Jorgensen, W. L. and Tirado-Rives, J.: The OPLS [Optimized Potentials for Liquid Simulations] Potential Functions for Proteins, Energy Minimizations for Crystals of Cyclic Peptides and Crambin, *J. Am. Chem. Soc.*, 110, 1657–1666, 1988.
- Jorgensen, W. L., Chandrasekhar, J., Madura, J. D., Impey, R. W., and Klein, M. L.: Comparison of Simple Potential Functions for Simulating Liquid Water, *J. Chem. Phys.*, 79, 926–935, 1983.
- Julin, J., Winkler, P., Donahue, N., Wagner, P., and Riipinen, I.: Near-Unity Mass Accommodation Coefficient of Organic Molecules of Varying Structure, *Environ. Sci. Technol.*, 48, 12083–12089, <https://doi.org/10.1021/es501816h>, 2014.
- Karnes, J. J. and Benjamin, I.: Geometric and energetic considerations of surface fluctuations during ion transfer across the water-immiscible organic liquid interface, *J. Chem. Phys.*, 145, 014701, <https://doi.org/10.1063/1.4954331>, 2016.
- Kertész, J., Darvas, M., Jedlovsky, P., and Horvai, G.: Reprint of “Role of the fluidity of a liquid phase in determining the surface properties of the opposite phase”, *J. Mol. Liq.*, 189, 122–128, <https://doi.org/10.1016/j.molliq.2013.06.009>, 2014.
- Klug, J., Triguero, C., Del Pópolo, M. G., and Tribello, G. A.: Using Intrinsic Surfaces To Calculate the Free-Energy Change When Nanoparticles Adsorb on Membranes, *J. Phys. Chem. B*, 122, 6417–6422, 2018.
- Krechmer, J. E., Day, D. A., Ziemann, P. J., and Jimenez, J. L.: Direct measurements of gas/particle partitioning and mass accommodation coefficients in environmental chambers, *Environ. Sci. Technol.*, 51, 11867–11875, 2017.
- Krieger, U. K., Marcolli, C., and Reid, J. P.: Exploring the complexity of aerosol particle properties and processes using single particle techniques, *Chem. Soc. Rev.*, 41, 6631–6662, <https://doi.org/10.1039/C2CS35082C>, 2012.
- Lbadaoui-Darvas, M., Takahama, S., and Nenes, A.: video supplement for “Molecular scale description of interfacial mass transfer in phase separated aqueous secondary organic aerosol”, Zenodo, <https://doi.org/10.5281/zenodo.4902870>, 2021.
- Li, Y. Q., Davidovits, P., Kolb, C. E., and Worsnop, D. R.: Mass and Thermal Accommodation Coefficients of H₂O(g) on Liquid Water as a Function of Temperature, *J. Phys. Chem. A*, 105, 10627–10634, <https://doi.org/10.1021/jp012758q>, 2001.
- Lienhard, D. M., Huisman, A. J., Krieger, U. K., Rudich, Y., Marcolli, C., Luo, B. P., Bones, D. L., Reid, J. P., Lambe, A. T., Canagaratna, M. R., Davidovits, P., Onasch, T. B., Worsnop, D. R., Steimer, S. S., Koop, T., and Peter, T.: Viscous organic aerosol particles in the upper troposphere: diffusivity-controlled water uptake and ice nucleation?, *Atmos. Chem. Phys.*, 15, 13599–13613, <https://doi.org/10.5194/acp-15-13599-2015>, 2015.
- Liu, D., Zhang, Y., Liu, Y., Wu, J., Chen, C.-C., Mou, C.-Y., and Chen, S.-H.: Density measurement of 1-D confined water by small angle neutron scattering method: pore size and hydration level dependences, *J. Phys. Chem. B*, 112, 4309–4312, 2008.
- Liu, P., Song, M., Zhao, T., Gunthe, S. S., Ham, S., He, Y., Qin, Y. M., Gong, Z., Amorim, J. C., Bertram, A. K., and Martin, S. T.: Resolving the mechanisms of hygroscopic growth and cloud condensation nuclei activity for organic particulate matter, *Nat. Commun.*, 9, 4076, <https://doi.org/10.1038/s41467-018-06622-2>, 2018.
- Liu, X., Day, D. A., Krechmer, J. E., Brown, W., Peng, Z., Ziemann, P. J., and Jimenez, J. L.: Direct measurements of semi-volatile organic compound dynamics show near-unity mass accommo-

- dation coefficients for diverse aerosols, *Commun. Chem.*, 2, 98, <https://doi.org/10.1038/s42004-019-0200-x>, 2019.
- Makowski, M. J., Stern, A. C., Hemminger, J. C., and Tobias, D. J.: Orientation and Structure of Acetonitrile in Water at the Liquid–Vapor Interface: A Molecular Dynamics Simulation Study, *J. Phys. Chem. C*, 120, 17555–17563, <https://doi.org/10.1021/acs.jpcc.6b05448>, 2016.
- Martin, M. G. and Siepmann, J. I.: Calculating Gibbs free energies of transfer from Gibbs ensemble Monte Carlo simulations, *Theor. Chem. Acc.*, 99, 347–350, 1998.
- Matsumoto, M., Saito, S., and Ohmine, I.: Molecular dynamics simulation of the ice nucleation and growth process leading to water freezing, *Nature*, 416, 409–413, 2002.
- Mauersberger, K. and Krankowsky, D.: Vapor Pressure above Ice at Temperatures below 170 K, *Geophys. Res. Lett.*, 30, 1121, <https://doi.org/10.1029/2002GL016183>, 2003.
- Miles, R. E. H., Davies, J. F., and Reid, J. P.: The influence of the surface composition of mixed monolayer films on the evaporation coefficient of water, *Phys. Chem. Chem. Phys.*, 18, 19847–19858, <https://doi.org/10.1039/C6CP03826C>, 2016.
- Moore, R. H., Raatikainen, T., Langridge, J. M., Bahreini, R., Brock, C. A., Holloway, J. S., Lack, D. A., Middlebrook, A. M., Perring, A. E., Schwarz, J. P., et al.: CCN spectra, hygroscopicity, and droplet activation kinetics of secondary organic aerosol resulting from the 2010 Deepwater Horizon oil spill, *Environ. Sci. Technol.*, 46, 3093–3100, 2012.
- Morales Betancourt, R. and Nenes, A.: Understanding the contributions of aerosol properties and parameterization discrepancies to droplet number variability in a global climate model, *Atmos. Chem. Phys.*, 14, 4809–4826, <https://doi.org/10.5194/acp-14-4809-2014>, 2014.
- Morita, A., Sugiyama, M., Kameda, H., Koda, S., and Hanson, D. R.: Mass Accommodation Coefficient of Water: Molecular Dynamics Simulation and Revised Analysis of Droplet Train/Flow Reactor Experiment, *J. Phys. Chem. B*, 108, 9111–9120, <https://doi.org/10.1021/jp030479s>, 2004.
- Murphy, D. M. and Koop, T.: Review of the vapour pressures of ice and supercooled water for atmospheric applications, *Quarterly Journal of the Royal Meteorological Society: A journal of the atmospheric sciences*, *Appl. Meteorol. Phys. Oceanogr.*, 131, 1539–1565, 2005.
- Nozière, B.: Don't forget the surface, *Science*, 351, 1396–1397, <https://doi.org/10.1126/science.aaf3253>, 2016.
- Ovadnevaite, J., Zuend, A., Laaksonen, A., Sanchez, K. J., Roberts, G., Ceburnis, D., Decesari, S., Rinaldi, M., Hodas, N., Facchini, M. C., Seinfeld, J. H., and O'Dowd, C.: Surface tension prevails over solute effect in organic-influenced cloud droplet activation, *Nature*, 546, 637–641, <https://doi.org/10.1038/nature22806>, 2017.
- Pajunoja, A., Lambe, A. T., Hakala, J., Rastak, N., Cummings, M. J., Brogan, J. F., Hao, L., Paramonov, M., Hong, J., Prisle, N. L., Malila, J., Romakkaniemi, S., Lehtinen, K. E. J., Laaksonen, A., Kulmala, M., Massoli, P., Onasch, T. B., Donahue, N. M., Riipinen, I., Davidovits, P., Worsnop, D. R., Petäjä, T., and Virtanen, A.: Adsorptive uptake of water by semisolid secondary organic aerosols, *Geophys. Res. Lett.*, 42, 3063–3068, <https://doi.org/10.1002/2015GL063142>, 2015.
- Park, S. and Schulten, K.: Calculating potentials of mean force from steered molecular dynamics simulation, *J. Chem. Phys.*, 120, 5946–5961, <https://doi.org/10.1063/1.1651473>, 2004.
- Pártay, L. B., Jedlovsky, P., Vincze, A., and Horvai, G.: Properties of Free Surface of Water–Methanol Mixtures. Analysis of the Truly Interfacial Molecular Layer in Computer Simulation, *J. Phys. Chem. B*, 112, 5428–5438, <https://doi.org/10.1021/jp711547e>, 2008.
- Petters, M. D., Kreidenweis, S. M., Snider, J. R., Koehler, K. A., Wang, Q., Prenni, A. J., and Demott, P. J.: Cloud droplet activation of polymerized organic aerosol, *Tellus B*, 58, 196–205, <https://doi.org/10.1111/j.1600-0889.2006.00181.x>, 2006.
- Piaggi, P. M. and Parrinello, M.: Predicting polymorphism in molecular crystals using orientational entropy, *P. Natl. Acad. Sci. USA*, 115, 10251–10256, <https://doi.org/10.1073/pnas.1811056115>, 2018.
- Poják, K., Darvas, M., Horvai, G., and Jedlovsky, P.: Properties of the Liquid–Vapor Interface of Water–Dimethyl Sulfoxide Mixtures, A Molecular Dynamics Simulation and ITIM Analysis Study, *J. Phys. Chem. C*, 114, 12207–12220, <https://doi.org/10.1021/jp101442m>, 2010.
- Potterton, A., Hussein, F. S., Southey, M. W. Y., Bodkin, M. J., Heifetz, A., Coveney, P. V., and Townsend-Nicholson, A.: Ensemble-Based Steered Molecular Dynamics Predicts Relative Residence Time of A2A Receptor Binders, *J. Chem. Theor. Comp.*, 15, 3316–3330, <https://doi.org/10.1021/acs.jctc.8b01270>, 2019.
- Prenni, A. J., Petters, M. D., Kreidenweis, S. M., DeMott, P. J., and Ziemann, P. J.: Cloud droplet activation of secondary organic aerosol, *J. Geophys. Res.*, 112, D10223, <https://doi.org/10.1029/2006JD007963>, 2007.
- Pruppacher, H. and Klett, J.: *Microstructure of Atmospheric Clouds and Precipitation*, Springer Netherlands, Dordrecht, 10–73, https://doi.org/10.1007/978-0-306-48100-0_2, 2010.
- Raatikainen, T., Nenes, A., Seinfeld, J. H., Morales, R., Moore, R. H., Latham, T. L., Lance, S., Padró, L. T., Lin, J. J., Cerully, K. M., Bougiatioti, A., Cozic, J., Ruehl, C. R., Chuang, P. Y., Anderson, B. E., Flagan, R. C., Jonsson, H., Mihalopoulos, N., and Smith, J. N.: Worldwide data sets constrain the water vapor uptake coefficient in cloud formation, *P. Natl. Acad. Sci. USA*, 110, 3760–3764, <https://doi.org/10.1073/pnas.1219591110>, 2013.
- Raznjevic, K.: *Handbook of thermodynamic tables and charts*, 1976.
- Renbaum-Wolff, L., Song, M., Marcolli, C., Zhang, Y., Liu, P. F., Grayson, J. W., Geiger, F. M., Martin, S. T., and Bertram, A. K.: Observations and implications of liquid–liquid phase separation at high relative humidities in secondary organic material produced by α -pinene ozonolysis without inorganic salts, *Atmos. Chem. Phys.*, 16, 7969–7979, <https://doi.org/10.5194/acp-16-7969-2016>, 2016.
- Rowlinson, J. S. J. S.: *Molecular theory of capillarity*, edited by: Rowlinson, J. S. and Widom, B., International series of monographs on chemistry, Clarendon Press, Oxford, UK, 1982.
- Roy, S., Diveky, M. E., and Signorell, R.: Mass Accommodation Coefficients of Water on Organics from Complementary Photoacoustic and Light Scattering Measurements on Laser-Trapped Droplets, *J. Phys. Chem. C*, 124, 2481–2489, <https://doi.org/10.1021/acs.jpcc.9b09934>, 2020.

- Ruehl, C. R., Chuang, P. Y., Nenes, A., Cappa, C. D., Kolesar, K. R., and Goldstein, A. H.: Strong evidence of surface tension reduction in microscopic aqueous droplets, *Geophys. Res. Lett.*, 39, L23801, <https://doi.org/10.1029/2012GL053706>, 2012.
- Ruehl, C. R., Davies, J. F., and Wilson, K. R.: An interfacial mechanism for cloud droplet formation on organic aerosols, *Science*, 351, 1447–1450, <https://doi.org/10.1126/science.aad4889>, 2016.
- Sakaguchi, S. and Morita, A.: Mass accommodation mechanism of water through monolayer films at water/vapor interface, *J. Chem. Phys.*, 137, 064701, <https://doi.org/10.1063/1.4740240>, 2012.
- Saleh, R., Donahue, N. M., and Robinson, A. L.: Time Scales for Gas-Particle Partitioning Equilibration of Secondary Organic Aerosol Formed from Alpha-Pinene Ozonolysis, *Environ. Sci. Technol.*, 47, 5588–5594, <https://doi.org/10.1021/es400078d>, 2013.
- Sareen, N., Schwier, A. N., Lathem, T. L., Nenes, A., and McNeill, V. F.: Surfactants from the gas phase may promote cloud droplet formation, *P. Natl. Acad. Sci. USA*, 110, 2723–2728, <https://doi.org/10.1073/pnas.1204838110>, 2013.
- Schmedding, R., Rasool, Q. Z., Zhang, Y., Pye, H. O. T., Zhang, H., Chen, Y., Surratt, J. D., Lopez-Hilfiker, F. D., Thornton, J. A., Goldstein, A. H., and Vizuete, W.: Predicting secondary organic aerosol phase state and viscosity and its effect on multiphase chemistry in a regional-scale air quality model, *Atmos. Chem. Phys.*, 20, 8201–8225, <https://doi.org/10.5194/acp-20-8201-2020>, 2020.
- Schöll-Paschinger, E. and Dellago, C.: A proof of Jarzynski's nonequilibrium work theorem for dynamical systems that conserve the canonical distribution, *J. Chem. Phys.*, 125, 054105, <https://doi.org/10.1063/1.2227025>, 2006.
- Sega, M., Hantal, G., Fábrián, B., and Jedlovsky, P.: Pytim: A python package for the interfacial analysis of molecular simulations, *J. Comput. Chem.*, 39, 2118–2125, <https://doi.org/10.1002/jcc.25384>, 2018.
- Shiraiwa, M. and Pöschl, U.: Mass accommodation and gas-particle partitioning in secondary organic aerosols: dependence on diffusivity, volatility, particle-phase reactions, and penetration depth, *Atmos. Chem. Phys.*, 21, 1565–1580, <https://doi.org/10.5194/acp-21-1565-2021>, 2021.
- Shiraiwa, M., Pfrang, C., Koop, T., and Pöschl, U.: Kinetic multi-layer model of gas-particle interactions in aerosols and clouds (KM-GAP): linking condensation, evaporation and chemical reactions of organics, oxidants and water, *Atmos. Chem. Phys.*, 12, 2777–2794, <https://doi.org/10.5194/acp-12-2777-2012>, 2012.
- Shiraiwa, M., Zuend, A., Bertram, A. K., and Seinfeld, J. H.: Gas-particle partitioning of atmospheric aerosols: interplay of physical state, non-ideal mixing and morphology, *Phys. Chem. Chem. Phys.*, 15, 11441–11453, <https://doi.org/10.1039/C3CP51595H>, 2013.
- Shiraiwa, M., Li, Y., Tsimpidi, A. P., Karydis, V. A., Berkemeier, T., Pandis, S. N., Lelieveld, J., Koop, T., and Pöschl, U.: Global distribution of particle phase state in atmospheric secondary organic aerosols, *Nat. Commun.*, 8, 1–7, 2017.
- Song, M., Marcolli, C., Krieger, U. K., Zuend, A., and Peter, T.: Liquid-liquid phase separation in aerosol particles: Dependence on O:C, organic functionalities, and compositional complexity, *Geophys. Res. Lett.*, 39, L19801, <https://doi.org/10.1029/2012GL052807>, 2012.
- Song, M., Liu, P., Martin, S. T., and Bertram, A. K.: Liquid-liquid phase separation in particles containing secondary organic material free of inorganic salts, *Atmos. Chem. Phys.*, 17, 11261–11271, <https://doi.org/10.5194/acp-17-11261-2017>, 2017.
- Takahama, S. and Russell, L. M.: A molecular dynamics study of water mass accommodation on condensed phase water coated by fatty acid monolayers, *J. Geophys. Res.-Atmos.*, 116, D02203, <https://doi.org/10.1029/2010JD014842>, 2011.
- Takamuku, T., Tabata, M., Yamaguchi, A., Nishimoto, J., Kumamoto, M., Wakita, H., and Yamaguchi, T.: Liquid Structure of Acetonitrile–Water Mixtures by X-ray Diffraction and Infrared Spectroscopy, *J. Phys. Chem. B*, 102, 8880–8888, <https://doi.org/10.1021/jp9824297>, 1998.
- Taylor, R. S. and Garrett, B. C.: Accommodation of alcohols by the liquid/vapor interface of water: Molecular dynamics study, *J. Phys. Chem. B*, 103, 844–851, 1999.
- Torrie, G. and Valleau, J.: Nonphysical sampling distributions in Monte Carlo free-energy estimation: Umbrella sampling, *J. Comput. Phys.*, 23, 187–199, [https://doi.org/10.1016/0021-9991\(77\)90121-8](https://doi.org/10.1016/0021-9991(77)90121-8), 1977.
- Tribello, G. A., Bonomi, M., Branduardi, D., Camilloni, C., and Bussi, G.: PLUMED 2: New Feathers for an Old Bird, *Comput. Phys. Commun.*, 185, 604–613, 2014.
- Truhlar, D. G. and Garrett, B. C.: Multidimensional Transition State Theory and the Validity of Grote-Hynes Theory, *J. Phys. Chem. B*, 104, 1069–1072, 2000.
- Tuckerman, M.: Statistical mechanics: theory and molecular simulation, Oxford University Press, Oxford, UK, 2010.
- Vargaftik, N., Volkov, B., and Voljak, L.: International tables of the surface tension of water, *J. Phys. Chem. Ref. Data*, 12, 817–820, 1983.
- Vega, C., Abascal, J., and Nezbeda, I.: Vapor-liquid equilibria from the triple point up to the critical point for the new generation of TIP4P-like models: TIP4P/Ew, TIP4P/2005, and TIP4P/ice, *J. Chem. Phys.*, 125, 34503, <https://doi.org/10.1063/1.2215612>, 2006.
- Vieceli, J., Roeselová, M., Potter, N., Dang, L. X., Garrett, B. C., and Tobias, D. J.: Molecular Dynamics Simulations of Atmospheric Oxidants at the Air–Water Interface: Solvation and Accommodation of OH and O₃, *J. Phys. Chem. B*, 109, 15876–15892, <https://doi.org/10.1021/jp051361>, 2005.
- Voigtländer, J., Stratmann, F., Niedermeier, D., Wex, H., and Kiselev, A.: Mass accommodation coefficient of water: A combined computational fluid dynamics and experimental data analysis, *J. Geophys. Res.-Atmos.*, 112, D20208, <https://doi.org/10.1029/2007JD008604>, 2007.
- von Domaros, M., Lakey, P. S. J., Shiraiwa, M., and Tobias, D. J.: Multiscale Modeling of Human Skin Oil-Induced Indoor Air Chemistry: Combining Kinetic Models and Molecular Dynamics, *J. Phys. Chem. B*, 124, 3836–3843, <https://doi.org/10.1021/acs.jpcc.0c02818>, pMID: 32290653, 2020.
- Ward, C.: Liquid-Vapour Phase Change Rates and Interfacial Entropy Production, *J. Non-Equil. Thermodyn.*, 27, 289–303, <https://doi.org/10.1515/JNETDY.2002.017>, 2002.
- Wendler, K., Thar, J., Zahn, S., and Kirchner, B.: Estimating the Hydrogen Bond Energy, *J. Phys. Chem. A*, 114, 9529–9536, <https://doi.org/10.1021/jp103470e>, pMID: 20707378, 2010.

- Wexler, A. et al.: Vapor pressure formulation for ice, *J. Res. Natl. Bur. Stand. A*, 81, 5–20, 1977.
- Wick, C. D., Siepmann, J. I., and Schure, M. R.: Temperature Dependence of Transfer Properties: Importance of Heat Capacity Effects, *J. Phys. Chem. B*, 107, 10623–10627, <https://doi.org/10.1021/jp0223556>, 2003.
- You, Y., Smith, M. L., Song, M., Martin, S. T., and Bertram, A. K.: Liquid–liquid phase separation in atmospherically relevant particles consisting of organic species and inorganic salts, *Int. Rev. Phys. Chem.*, 33, 43–77, 2014.
- Zielkiewicz, J.: Structural properties of water: Comparison of the SPC, SPCE, TIP4P, and TIP5P models of water, *J. Chem. Phys.*, 123, 104501, <https://doi.org/10.1063/1.2018637>, 2005.
- Zientara, M., Jakubczyk, D., Kolwas, K., and Kolwas, M.: Temperature Dependence of the Evaporation Coefficient of Water in Air and Nitrogen under Atmospheric Pressure: Study in Water Droplets, *J. Phys. Chem. A*, 112, 5152–5158, <https://doi.org/10.1021/jp7114324>, 2008.